Dynamic strain localization into a compaction band via a phase-field approach

Yunteng Wang[1], Ronaldo I. Borja[2], Wei Wu[1,*],

[1]Institut für Geotechnik, Universität für Bodenkultur Wien, 1180 Vienna, Austria
[2]Department of Civil and Environmental Engineering, Stanford University, California 94305, USA
[*]E-mail: `wei.wu@boku.ac.at`

Summary. We present a new phase-field formulation for the formation and propagation of a compaction band in high-porosity rocks. Novel features of the proposed formulation include (a) the effects of inertia on the rate of development of compaction bands, and (b) degradation mechanisms in tension, compression, and shear appropriate for dynamic strain localization problems where disturbances propagate in time in a wave-like fashion to induce micro-cracking, grain crushing, and frictional grain rearrangement in the rock. We also present a robust numerical technique to handle the spatiotemporal formation and evolution of the compaction band. We validate the model by simulating a benchmark problem involving a V-shape notched cylindrical specimen of Bentheim sandstone tested in conventional triaxial compression. The model is shown to reproduce different geometric styles of deformation that include pure compaction, shear-enhanced compaction, and a combination of pure and shear-enhanced compaction, where the combination mechanism consists of a straight primary compaction band surrounded by secondary chevron bands.

Keywords. compaction band, dynamic strain localization, grain crushing, phase-field, shear band

1 Introduction

Localized deformation bands, including shear bands, dilation bands, compaction bands, and mixed-mode bands, are often observed in porous geologic media both in the laboratory and in the field [55]. They typically occur in sandstones [12, 86], limestones [16, 61], carbonates [14, 39, 98], and clay rocks [62, 64]. Compaction bands are narrow zones of intense deformation characterized by little or no shear offset (see Figures 1). Compaction bands are often oriented perpendicular to the direction of the maximum principal stress [33, 54, 84], but they can also be enhanced by shearing and develop obliquely with respect to the maximum principal stress [49, 58, 70]. Field observations and laboratory tests in porous rocks indicate that the occurrence of compaction bands is usually accompanied by significant permeability reduction, which plays a critical role in prospecting hydrocarbon reservoirs, CO_2 storage, and hazardous waste disposal [59, 87, 92, 100].

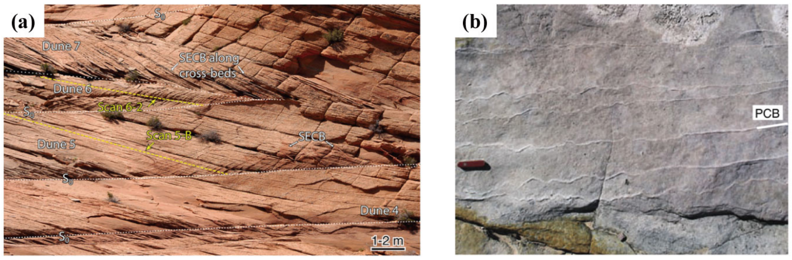

Fig. 1. Geological evidences of (a) shear-enhanced compaction bands [54] and (b) pure compaction bands [49] from *in-situ* field-scale observations. Abbreviations: SECB = shear-enhanced compaction band; PCB = pure compaction band.

Over the last decades, compaction bands in high-porosity rocks have been the subject of extensive experimental studies [1, 12, 14, 16, 61, 69, 75, 107, 110], field investigations [33, 54, 55, 84], and theoretical and numerical analyses [11, 22, 66, 88, 90, 102]. Insights into the origin of this intriguing deformation style in rocks have improved significantly through laboratory testing and field observations. The incipience of a compaction band is well captured by most theoretical and numerical models, but its evolution beyond the initiation stage has continued to challenge the theoretical and computational modelers. Many conventional finite element models lack a characteristic length scale that inevitably results in spurious mesh dependence. Moreover, recent experimental observations suggest that the formation of compaction bands is characterized by two concurrent dissipation mechanisms, namely, plastic deformation and brittle/ductile fracture. In most models, only plastic dissipation is considered [2, 23, 42–44, 77]. Discrete element methods (DEM) have been used to model brittle/ductile fracture as it relates to the development of a compaction band [32, 48, 78, 85, 104, 113, 116], but they are only appropriate for grain-scale simulations and have difficulty reproducing macroscopic deformation styles observed in the field. Meshless methods such as the smoothed particle hydrodynamics (SPH) have also been employed to capture the kinematics of shear bands [45, 46], but not that of compaction bands.

Regularized energy-based numerical methods such as the gradient-enhanced method and the phase-field approach [28, 56, 64, 80, 81, 112] have offered appealing alternatives for simulating the failure processes in solid materials [3, 4, 47, 105, 106, 114, 119]. In particular, the phase-field approach possesses distinct advantages over other numerical techniques due to its standard variational form [56, 80] that allows propagation of the discontinuity without requiring a special band tracing technique [20, 21, 24, 71, 72]. In the phase-field approach, the discontinuous field such as a fracture or a deformation band is regularized by a more diffuse damage zone through a phase-field variable d and an internal length scale ℓ, where the latter can also serve to bridge the gap between the microscopic and macroscopic properties of the material. Moreover, in the phase-field approach the discontinuous field can be propagated without recourse to *ad hoc* criteria. Because of these advantages, the phase-field approach has now been used to address many discontinuous problems in solid mechanics, as well as to model the failure behavior of solid materials including concrete [34, 52], rocks [30, 51, 51, 73, 129], and composites [89, 123].

Early works on phase-field modeling have focused mainly on the simulation of brittle failure. In 2015, Ambati et al. [5] published one of the first articles to address ductile failure within the phase-field framework. They initially developed the framework at infinitesimal strains, but later extended it to finite strains [6, 10] and combined the formulation with gradient plasticity-damage theory [83]. Borden et al. [19] proposed a phase-field model to study the effects of plastic degradation function on ductile fracture. Meanwhile, several phase-field models with elastoplasticity were also proposed to simulate the brittle-to-ductile failure phenomena [37, 79, 82, 115, 117] and shear band formation [9, 118, 122, 124]. In these aforementioned works, only metallic materials were considered along with deviatoric plasticity [25].

More recent applications of the phase-field theory have focused on the capture of localized deformation in geologic materials. Choo and co-workers [35, 36, 50, 51] considered the phase-field evolution of discontinuous media with pressure-sensitive plasticity to capture a wide range of failure modes from brittle fracture to ductile flow. Wang et al. [111] derived the driving force characterizing the phase-field evolution based on the Mohr–Coulomb criterion for pressure-sensitive materials. You et al. [121] considered the plastic work to develop a modified phase-field damage model simulating the brittle-to-ductile failure transition. Hu et al. [60] proposed a hybrid phase-field model based on an implicit material point method for brittle-ductile fracture transition in geomaterials. In addition, the phase-field approach has also been coupled with fluid flow in recent works [103, 120]. However, most of the above works have focused only on the fracture and shear band formation in geologic media, and none has addressed the problem of compaction bands.

Most recently, Ip and Borja [64] proposed a phase-field approach for compaction band formation and propagation in rocks employing breakage mechanics and critical state plasticity. Their approach involves the solution of an elliptic partial differential equation (PDE) in the context of quasi-static loading and rate-independent elastoplasticity. They introduced a degradation function for deformation in compaction and shear to represent pore collapse mechanisms in both the elastic and plastic responses. We pick up from their work and present an alternative phase-field approach incorporating dynamic effects for compaction band formation and propagation in high-porosity rocks.

Dynamic strain localization involves the solution of a hyperbolic PDE in which the disturbances propagate in time in a wave-like fashion. The stress points within the problem domain could experience both compression and extension as the disturbance propagates, even if the overall response of the rock is dominated by compressive deformation, making the dynamic solution distinct from a quasi-static solution. We thus introduce separate degradation functions in compression, extension, and shear to capture the various deformation mechanisms leading to the formation and propagation of a deformation band. We show that the proposed model is equally capable of simulating different patterns and geometric styles of localized deformation, including those not previously observed in quasi-static simulations of compaction bands.

The structure of presentation is as follows. Section 2 presents the proposed phase-field formulation. Section 3 develops the numerical solution strategy. Section 4 solves a benchmark example of compaction band formation in a sandstone, while Section 5 discusses several other numerical examples. Finally, Section 6 presents the conclusions derived from this work.

2 Phase-field formulation

This section presents the proposed phase-field theory for a deformation band in general and compaction band in particular. We first formulate the equations characterizing the geometry and evolution of the band. Then, we present a constitutive theory appropriate for characterizing the band formation and propagation.

2.1 Phase-field characterization of a deformation band

We consider an arbitrary solid body $\mathcal{B} \subseteq \mathbb{R}^n$ in the reference configuration, where n denotes the spatial dimension. We assume that $\mathcal{B}$ contains an internal discontinuity Γ that is approximated by the phase field variable $d\,(\boldsymbol{x}, t) \in [0, 1]$. Figures 2(a) and 2(b) depict such a prototype discontinuity Γ_ℓ in the form of a deformation band with a diffuse topology and having a thickness of 2ℓ.

In the phase-field approach [80, 81, 118], the surface of discontinuity may include fractures (strong discontinuities) and deformation bands (weak discontinuities), and is represented by the expression

$$\Gamma_B = \int_\Gamma d\Gamma = \int_{\mathcal{B}} \gamma\,(d, \nabla d)\, dV\,, \tag{1}$$

where $\gamma\,(d, \nabla d)$ denotes the discontinuous surface density function, whose distribution is given in terms of an internal characteristic length ℓ as

$$\gamma\,(d, \nabla d) = \frac{1}{2\ell} d^2 + \frac{\ell}{2} |\nabla d|^2\,. \tag{2}$$

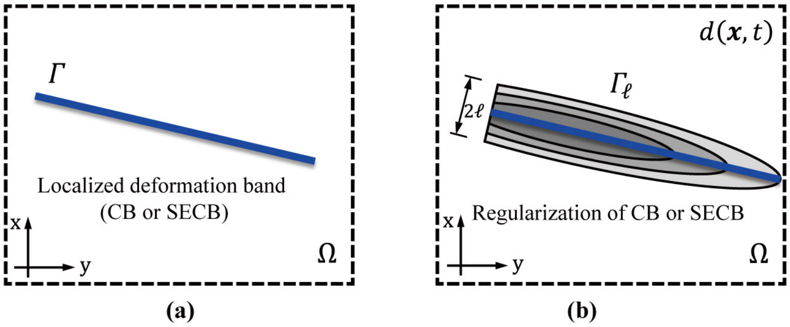

Fig. 2. Schematic diagrams of deformation bands: (a) sharp topology of localization zones and (b) the relevant phase-field regularized deformation bands. Abbreviations: CB = pure compaction band; SECB = shear-enhanced compaction band.

Let $\varPsi\left(\boldsymbol{\varepsilon},\boldsymbol{\alpha}\right)$ be the total free energy function in $\mathcal{B}$, where $\boldsymbol{\varepsilon}$ is the infinitesimal strain tensor and $\boldsymbol{\alpha}$ is the vector of strain-like plastic internal variables. In the presence of a deformation band, the regularized form of $\varPsi$, denoted as $\varPsi_\ell$, may be developed by introducing the phase-field variable d and its gradient ∇d as follows (see [28])

$$\begin{aligned}\varPsi_\ell\left(\boldsymbol{\varepsilon},\boldsymbol{\alpha},d,\nabla d\right) &= \varPsi_o\left(\boldsymbol{\varepsilon},\boldsymbol{\alpha},d\right)+\varPsi_i\left(d,\nabla d\right)\\ &= \int_{\mathcal{B}}\psi_o\left(\boldsymbol{\varepsilon},\boldsymbol{\alpha},d\right)dV+\int_{\mathcal{B}}\psi_i\left(d,\nabla d\right)dV\,, \end{aligned}\tag{3}$$

where $\varPsi_o$ and $\varPsi_i$ are the total free energies “outside” and “inside” the band, respectively,

$$\psi_i\left(d,\nabla d\right)=\mathcal{G}_c\gamma\left(d,\nabla d\right)\,,\tag{4}$$

and $\mathcal{G}_c$ is the fracture energy release rate associated with plastic dissipation and band “toughness” [57, 91]. The free energy $\varPsi_i\left(d,\nabla d\right)$ represents the energy that is released as a result of the formation of the deformation band, while $\varPsi_o\left(\boldsymbol{\varepsilon},\boldsymbol{\alpha},d\right)$ is the energy associated with the deformation of the body as a whole.

Based on the assumption of elastic energy depending only on the elastic strains and the plastic energy depending only on the plastic strains [40, 76, 130], the free energy density ψ_o can be decomposed into the following form:

$$\psi_o\left(\boldsymbol{\varepsilon},\boldsymbol{\alpha},d\right)=\psi_o^e\left(\boldsymbol{\varepsilon}^e,d\right)+\psi_o^p\left(\boldsymbol{\varepsilon}^p,\boldsymbol{\alpha},d\right)\,,\tag{5}$$

where ψ_o^e and ψ_o^p denote the elastic and plastic parts of ψ_o, respectively. For isothermal process, the second law of thermodynamics can then be stated in the form of the Clausius-Planck inequality [99, 109] as

$$\boldsymbol{\sigma}:\dot{\boldsymbol{\varepsilon}}-\dot{\psi}_o^e\geq 0\,.\tag{6}$$

The dissipation function can then be written as

$$\mathcal{D}^p = \dot{\psi}_o^p + \dot{\psi}_i \geq 0\,. \tag{7}$$

The first term on the right-hand side of (7) represents the plastic dissipation in the bulk volume whereas the second term represents the plastic dissipation due to the formation and propagation of the deformation band.

2.2 Driving force

In the phase-field formulation, the energetic forces of the constitutive model drive the evolution of the phase-field variable [5, 82, 111, 112]. For quasi-brittle materials, the energy balance can be expressed by setting the rate of band deformation as a function of the power of the driving force [82, 111].

We first quantify the geometry and evolution of the deformation band as follows. Taking the time-derivative of (1) yields

$$\dot{\mathit{\Gamma}}_B\,(d) = \int_{\mathcal{B}} \dot{\gamma}\, dV = \frac{1}{\ell}\int_{\mathcal{B}} d\dot{d}\, dV + \ell \int_{\mathcal{B}} \nabla d \cdot \nabla \dot{d}\, dV\,. \tag{8}$$

Noting that

$$\nabla d \cdot \nabla \dot{d} = \nabla \cdot (\nabla d \dot{d}) - (\nabla^2 d)\dot{d}\,, \tag{9}$$

we can insert this last equation into (8) and use the divergence theorem to obtain

$$\dot{\mathit{\Gamma}}_B(d) = \frac{1}{\ell}\int_{\mathcal{B}} (d - \ell^2\nabla^2 d)\dot{d}\, dV + \ell \int_{\partial\mathcal{B}} (\nabla d \cdot \boldsymbol{n})\dot{d}\, dA\,. \tag{10}$$

In the phase-field formulation, the boundary condition on the phase-field variable takes the form

$$\nabla d \cdot \boldsymbol{n} = 0 \;\text{ on } \partial\mathcal{B}\,. \tag{11}$$

Thus, the evolution of the deformation band simplifies to

$$\dot{\mathit{\Gamma}}_B(d) = \frac{1}{\ell}\int_{\mathcal{B}} (d - \ell^2\nabla^2 d)\dot{d}\, dV\,. \tag{12}$$

We next assume that $\dot{\mathit{\Gamma}}_B$ is induced by some net driving force of the form given by (see [82])

$$\dot{\mathit{\Gamma}}_B = \frac{1}{\ell}\int_{\mathcal{B}} \left[\mathcal{H}^{\mathrm{eq}}\left(\boldsymbol{\varepsilon}, \boldsymbol{\varepsilon}^p, \boldsymbol{\alpha}, d\right) - \mathcal{R}\right] \cdot \dot{d}\, dV \tag{13}$$

Here, $\mathcal{H}^{\mathrm{eq}}\left(\boldsymbol{\varepsilon}, \boldsymbol{\varepsilon}^p, \boldsymbol{\alpha}, d\right)$ denotes a driving force responsible for the localization of deformation, while $\mathcal{R}$ is some viscous resistance of the form

$$\mathcal{R} = \zeta \dot{d}\,, \tag{14}$$

where ζ is a viscosity parameter. The strong form of the phase-field evolution for localized failure at any material point can then be written as

$$\zeta \dot{d} = \mathcal{H}^{\mathrm{eq}} \left(\boldsymbol{\varepsilon}, \boldsymbol{\varepsilon}^p, \boldsymbol{\alpha}, d\right) - \left(d - \ell^2 \nabla^2 d\right) \text{ in } \mathcal{B}\,, \tag{15}$$

subject to the boundary condition given in (11).

Due to the irreversibility of the deformation process, we need to impose the following constraints on the theory:

$$\left.\begin{aligned} d\left(\boldsymbol{x}, t\right) \in [0, 1] \\ \dot{d}\left(\boldsymbol{x}, t\right) \geq 0 \\ \mathcal{H}^{\mathrm{eq}}\left(\boldsymbol{\varepsilon}, \boldsymbol{\varepsilon}^p, \boldsymbol{\alpha}, d\right) \geq 0 \end{aligned}\right\} . \tag{16}$$

It is worth noting that in high-porosity rocks, the localized failure driving force $\mathcal{H}^{\mathrm{eq}}$ is related to both the elastic energetic and plastic deformation states, whereas the viscous resistance $\mathcal{R}$ simply depends on the time derivative of the phase-field variable d.

2.3 Degradation functions

Because the solutions of hyperbolic equations are "wave-like," degradation functions in both compressive and dilative types of deformation must be introduced to accommodate for damage in both modes even if the expected deformation is mostly compressive. In this work, we utilize the classic degradation functions for opening-mode fractures and enhance the description further by introducing another degradation function based on crushing potential for compressive types of deformation.

The classic degradation functions for opening-mode fractures are of the following form: For the elastic free energy, we assume small deformation and isothermal condition and decompose the total strain tensor $\boldsymbol{\varepsilon}$ additively into an elastic part $\boldsymbol{\varepsilon}^e$ and a plastic part $\boldsymbol{\varepsilon}^p$. In rate form, we have

$$\dot{\boldsymbol{\varepsilon}} = \dot{\boldsymbol{\varepsilon}}^e + \dot{\boldsymbol{\varepsilon}}^p. \tag{17}$$

We evaluate the von Mises equivalent plastic strain as

$$\varepsilon^p_{\mathrm{eq}} := \sqrt{\frac{2}{3}} \int_0^t \sqrt{\dot{\boldsymbol{\varepsilon}}^p : \dot{\boldsymbol{\varepsilon}}^p} d\tau\,, \tag{18}$$

and define

$$r = \frac{\varepsilon^p_{\mathrm{eq}}}{\varepsilon^p_{\mathrm{eq,crit}}} \tag{19}$$

as the normalized cumulative plastic strain, which attains a value 1.0 when the von Mises strain reaches a threshold value $\varepsilon^p_{\mathrm{eq,crit}}$. We incorporate r into the Helmholtz free energy as

$$\psi = \psi^e_o \left(\boldsymbol{\varepsilon}^e, r, d\right) + \psi^p_o \left(\boldsymbol{\varepsilon}^p, \boldsymbol{\alpha}, d\right) + \psi_i \left(d, \nabla d\right), \tag{20}$$

which leads to elastoplastic coupling on the elastic free energy.

We consider an elastic degradation function of the form

$$g_1(d,r) = (1-d)^{2r^m}, \tag{21}$$

where $m \in \{1,2,3,\ldots\}$ is an exponent that controls the 'speed' of localized failure mechanism [5]. In this work, we take $m = 1$. We also consider the following decomposition of the elastic strain tensor into volumetric and deviatoric parts,

$$\boldsymbol{\varepsilon}^e = \boldsymbol{\varepsilon}^e_{\text{vol}} + \boldsymbol{\varepsilon}^e_{\text{dev}}\,, \tag{22}$$

where $\boldsymbol{\varepsilon}^e_{\text{vol}}$ and $\boldsymbol{\varepsilon}^e_{\text{dev}}$ are the volumetric and deviatoric parts, respectively. Taking the purely dilatational part ψ^{e+}_{vol}, purely compressive part ψ^{e-}_{vol}, and mixed tensile/compressive-shear deformation part ψ^e_{dev} into consideration, the stored elastic energy density is then written as (see [7, 73]).

$$\psi^e_o\left(\boldsymbol{\varepsilon}^e,r,d\right) = \psi^{e+}_{\text{vol}}\left(\boldsymbol{\varepsilon}^e,r,d\right) + \psi^e_{\text{dev}}\left(\boldsymbol{\varepsilon}^e,r,d\right) + \psi^{e-}_{\text{vol}}\left(\boldsymbol{\varepsilon}^e,r,d\right)\,, \tag{23}$$

where

$$\left.\begin{aligned} \psi^{e+}_{\text{vol}}\left(\boldsymbol{\varepsilon}^e,r,d\right) &= g_1\left(d,r\right)\frac{K^e}{2}\text{tr}^+(\boldsymbol{\varepsilon}^e)^2 \\ \psi^e_{\text{dev}}\left(\boldsymbol{\varepsilon}^e,r,d\right) &= g_1\left(d,r\right)\mu^e\boldsymbol{\varepsilon}^e_{\text{dev}}:\boldsymbol{\varepsilon}^e_{\text{dev}} \\ \psi^{e-}_{\text{vol}}\left(\boldsymbol{\varepsilon}^e,d,r\right) &= g_1(d,r)\theta\frac{K^e}{2}\text{tr}^-(\boldsymbol{\varepsilon}^e)^2 + (1-\theta)\frac{K^e}{2}\text{tr}^-(\boldsymbol{\varepsilon})^2 \end{aligned}\right\}\,, \tag{24}$$

K^e and μ^e are the elastic bulk and shear moduli of the intact material, $\text{tr}^+(\boldsymbol{\varepsilon}) = \max\{0,\text{tr}(\boldsymbol{\varepsilon})\}$ and $\text{tr}^-(\boldsymbol{\varepsilon}) = \min\{0,\text{tr}(\boldsymbol{\varepsilon})\}$ are adopted to prevent the interpenetration of failure surfaces in the compressive regions.

The parameter $\theta \in [0,1]$ in (24) is the crushing potential introduced by Ip and Borja [64] to degrade the elastic bulk modulus in compression. This parameter works in such a way that as $d \to 1$, the degraded elastic bulk modulus approaches a nonzero value $(1-\theta)K^e$. On the other hand, we note that the elastic bulk modulus in opening-mode fracture approaches zero as $d \to 1$. The Cauchy stress tensor $\boldsymbol{\sigma}$ can then be evaluated from the equation

$$\boldsymbol{\sigma} = \frac{\partial\psi^e_o}{\partial\boldsymbol{\varepsilon}^e} = g_1(d,r)\frac{\partial\psi^{e+}_o}{\partial\boldsymbol{\varepsilon}^e} + g_1(d,r)\theta\frac{\partial\psi^{e-}_{\text{vol}}}{\partial\boldsymbol{\varepsilon}^e} + (1-\theta)\frac{\partial\psi^{e-}_{\text{vol}}}{\partial\boldsymbol{\varepsilon}^e}\,, \tag{25}$$

where

$$\psi^{e+}_o = \frac{K^e}{2}\text{tr}^+(\boldsymbol{\varepsilon}^e)^2 + \mu^e\boldsymbol{\varepsilon}^e_{\text{dev}}:\boldsymbol{\varepsilon}^e_{\text{dev}}\,. \tag{26}$$

We next turn to the plastic free energy. Employing the same decomposition of the plastic strain rate into volumetric and deviatoric parts,

$$\dot{\boldsymbol{\varepsilon}}^p = \dot{\boldsymbol{\varepsilon}}^p_{\text{vol}} + \dot{\boldsymbol{\varepsilon}}^p_{\text{dev}}\,, \tag{27}$$

we can write the plastic energy density ψ^p_o as

$$\psi_o^p = \psi_{\text{vol}}^p + g_2(d)\psi_{\text{dev}}^p \, , \tag{28}$$

where

$$\psi_{\text{vol}}^p = \int_0^t \boldsymbol{\sigma} : \dot{\boldsymbol{\varepsilon}}_{\text{vol}}^p \, d\tau \, , \quad \psi_{\text{dev}}^p = \int_0^t \boldsymbol{\sigma} : \dot{\boldsymbol{\varepsilon}}_{\text{dev}}^p \, d\tau \, . \tag{29}$$

Here, g_2 is another degradation function defined by Bourdin et al. [28] of the form

$$g_2(d) = (1-d)^2 \, . \tag{30}$$

Note that whereas the degradation function $g_1(d, r)$ allows for the explicit dependence of the phase-field variable d on both the elastic and plastic strain energy densities, the degradation function $g_2(d)$ does not depend on the elastic strain and is a function solely of the phase-field variable d. Moreover, the two degradation functions account for energy dissipation by both brittle-like microcracking/grain crushing phenomena and plastic-driven failure/friction/grain arrangement during the deformation band processes, in agreement with the microscopic observations in the laboratory [1, 53].

Remark. Compared to the formulation by Ip and Borja [64], the degradation function g_2 employed in the present formulation is applied directly to the plastic work, whereas the degradation function used in the formulation of Ip and Borja is introduced into the evolution of the preconsolidation pressure to reflect the shift in the void-ratio versus logarithm of pressure curve due to pore collapse.

2.4 Evolution of the phase-field variable

We derive the evolution of the phase-field variable d from the regularized total potential energy given by the expression

$$\Pi_\ell = \Psi_\ell + \Upsilon + K - W \, , \tag{31}$$

where

$$\Psi_\ell = \int_{\mathcal{B}} \psi \, dV = \int_{\mathcal{B}} (\psi_o^e + \psi_o^p + \psi_i) \, dV \tag{32}$$

is the total free energy,

$$\Upsilon = \frac{\mathcal{G}_c}{\ell} \int_{\mathcal{B}} \mathcal{R} d \, dV \tag{33}$$

is the work done by the viscous force $\mathcal{R}$ in forming and propagating the band,

$$K = \int_{\mathcal{B}} \frac{1}{2} \rho \boldsymbol{v} \cdot \boldsymbol{v} \, dV \tag{34}$$

is the kinetic energy of the system, with ρ = mass density of the rock and $\boldsymbol{v}$ = velocity vector, and

$$W = \int_{\mathcal{B}} \rho \boldsymbol{g} \cdot \boldsymbol{v} \, dV + \int_{\partial \mathcal{B}} \boldsymbol{t} \cdot \boldsymbol{v} \, dA \tag{35}$$

is the external work done by the body force $\rho \boldsymbol{g}$ and surface traction $\boldsymbol{t}$.

Taking the stationary point of $\mathit{\Pi}_\ell$ with respect to $\boldsymbol{v}$, using the divergence theorem on the surface integral, and localizing yields the overall equilibrium condition

$$\frac{\partial \mathit{\Pi}_\ell}{\partial \boldsymbol{v}} = \boldsymbol{0} \quad \Longrightarrow \quad \nabla \cdot \boldsymbol{\sigma} + \rho \boldsymbol{g} = \rho \boldsymbol{a} \, , \tag{36}$$

where $\boldsymbol{a}$ is the material acceleration. Furthermore, taking the stationary point of $\mathit{\Pi}_\ell$ with respect to d and localizing gives the evolution condition for the phase-field variable

$$\frac{\partial \mathit{\Pi}_\ell}{\partial d} = 0 \quad \Longrightarrow \quad \mathcal{G}_c \ell \nabla^2 d - \mathcal{G}_c \frac{d}{\ell} - \frac{\partial \psi_o}{\partial d} = \frac{\mathcal{G}_d}{\ell} \zeta \dot{d} \, , \tag{37}$$

where

$$\frac{\partial \psi_o}{\partial d} = -2(1-d)^{2r-1} \left[r(\psi^{e+}_{\text{vol}} + \psi^{e}_{\text{dev}} + \theta \psi^{e-}_{\text{vol}}) \right] - 2(1-d) \psi^{p}_{\text{dev}} \, . \tag{38}$$

2.5 Plasticity model

Based on thermodynamics, the total stress tensor can be decomposed as

$$\boldsymbol{\sigma} = \boldsymbol{\xi} + \boldsymbol{\chi} \, , \tag{39}$$

where $\boldsymbol{\xi}$ is the shift and $\boldsymbol{\chi}$ denotes the dissipative stress tensors referring to Ziegler's orthogonality hypothesis [41, 67, 130]. In our phase-field model for localized deformation bands in geological media, the shift and dissipative stress tensors can be written as follows

$$\boldsymbol{\xi} = g_2(d) \frac{\partial \psi^{p}_{\text{dev}}(\boldsymbol{\varepsilon}^p, \boldsymbol{\alpha})}{\partial \boldsymbol{\varepsilon}^p} + \frac{\partial \psi^{p}_{\text{vol}}(\boldsymbol{\varepsilon}^p, \boldsymbol{\alpha})}{\partial \boldsymbol{\varepsilon}^p} \, , \tag{40}$$

$$\boldsymbol{\chi} = g_2(d) \frac{\partial \psi^{p}_{\text{dev}}(\boldsymbol{\varepsilon}^p, \boldsymbol{\alpha})}{\partial \boldsymbol{\alpha}} + \frac{\partial \psi^{p}_{\text{vol}}(\boldsymbol{\varepsilon}^p, \boldsymbol{\alpha})}{\partial \boldsymbol{\alpha}} \, . \tag{41}$$

For the dissipative stress space in elastoplasticity, the shift pressure $\hat{\rho}$ and dissipative pressure π can be calculated in the following forms to evaluate the plastic components of the deformation

$$\hat{\rho} = -\frac{1}{3} \text{tr}(\boldsymbol{\xi}) \, , \qquad \pi = -\frac{1}{3} \text{tr}(\boldsymbol{\chi}) \, , \tag{42}$$

which results in the effective pressure and the deviatoric stress invariant as follows

$$P = \hat{\rho} + \pi \, , \tag{43a}$$

$$Q = \mathcal{J}_2(\boldsymbol{\chi}) \, , \tag{43b}$$

where Q is the von Mises dissipative stress and the effective pressure P in compression is regarded as positive.

In this work, the local yield surface $\mathcal{F}(\pi, Q)$ in the dissipative stress space (π, Q) is adopted as [41]

$$\mathcal{F}(\pi, Q) = \sqrt{\frac{\pi^2}{A^2} + \frac{Q^2}{B^2}} - 1 \leq 0\,, \tag{44}$$

where A and B are coefficients defining the shape of the yield surface, which are given by the expressions [41]

$$A = (1-\gamma)\, P + \frac{1}{2}\gamma P_c \tag{45a}$$

$$B = \mu \left[(1-\alpha)\, P + \frac{1}{2}\alpha\gamma P_c\right]\,, \tag{45b}$$

in which μ, γ and α are dimensionless material constants. Moreover, in classical elastoplasticity the shift pressure is rewritten as

$$\hat{\rho} = \frac{1}{2}\gamma P_c^0 \exp\left(\frac{\varepsilon^p_{\text{vol}}}{\mathit{\Lambda}_c}\right) \tag{46}$$

where $\mathit{\Lambda}_c$ is the plastic compressibility and P_c^0 denotes the initial preconsolidation pressure.

In the effective dissipative stress space with an elliptical yield function $\mathcal{F}(\pi, Q)$, the flow rules of the plastic strain invariants are stated as follows

$$\dot{\varepsilon}^P = \dot{\lambda}\frac{\partial \mathcal{F}}{\partial \pi} = \frac{\langle \mathcal{F} \rangle}{\eta}\frac{\partial \mathcal{F}}{\partial \pi} = \frac{\langle \mathcal{F} \rangle}{\eta\,(1+\mathcal{F})}\frac{\pi}{A^2}\,, \tag{47a}$$

$$\dot{\varepsilon}^Q = \dot{\lambda}\frac{\partial \mathcal{F}}{\partial Q} = \frac{\langle \mathcal{F} \rangle}{\eta}\frac{\partial \mathcal{F}}{\partial Q} = \frac{\langle \mathcal{F} \rangle}{\eta\,(1+\mathcal{F})}\frac{Q}{B^2}\,, \tag{47b}$$

where η is the plastic viscosity with the specific unit of Pa^{-1}s, and $\langle \bullet \rangle := (\bullet + |\bullet|)/2$ are the Macaulay brackets.

2.6 Localized failure driving forces

Recalling the phase-field evolution of localized failure bands in (15), the localized failure driving force $\mathcal{H}^{\text{eq}}(\boldsymbol{\varepsilon}, \boldsymbol{\varepsilon}^p, \boldsymbol{\alpha}, d)$ is written as

$$\mathcal{H}^{\text{eq}}(\boldsymbol{\varepsilon}, \boldsymbol{\varepsilon}^p, \boldsymbol{\alpha}, d) = \mathcal{H}^e(\boldsymbol{\varepsilon}^e, r, d) + \mathcal{H}^p(\boldsymbol{\varepsilon}^p, \boldsymbol{\alpha}, d) \tag{48}$$

where $\mathcal{H}^e(\boldsymbol{\varepsilon}^e, r, d)$ and $\mathcal{H}^p(\boldsymbol{\varepsilon}^p, \boldsymbol{\alpha}, d)$ are the localized failure driving forces due to microcracking and plastic dissipations, respectively, which are explicitly calculated as

$$\begin{aligned} \mathcal{H}^e(\boldsymbol{\varepsilon}^e, r, d) &= \mathcal{H}^{e+}_{\text{vol}}(\boldsymbol{\varepsilon}^e, r, d) + \mathcal{H}^e_{\text{dev}}(\boldsymbol{\varepsilon}^e, r, d) \\ &= \max_{0\leq t\leq T}\left\{\boldsymbol{\sigma}(\boldsymbol{\varepsilon}^e, d) : \boldsymbol{\varepsilon}^{e+}_{\text{vol}} + \boldsymbol{\sigma}(\boldsymbol{\varepsilon}^e, d) : \boldsymbol{\varepsilon}^e_{\text{dev}}\right\} \end{aligned} \tag{49}$$

and

$$\mathcal{H}^p\left(\boldsymbol{\varepsilon}^p, \boldsymbol{\alpha}, d\right) = \mathcal{H}^{p+}_{\text{vol}}\left(\boldsymbol{\varepsilon}^p, \boldsymbol{\alpha}, d\right) + \mathcal{H}^{p}_{\text{dev}}\left(\boldsymbol{\varepsilon}^p, \boldsymbol{\alpha}, d\right) = \int_0^t \boldsymbol{\sigma}\left(\varepsilon^e, d\right) : \left(\dot{\boldsymbol{\varepsilon}}^{p+}_{\text{vol}} + \dot{\boldsymbol{\varepsilon}}^{p}_{\text{dev}}\right) d\tau \,. \tag{50}$$

3 Finite element implementation

The standard finite element method is used in this work. The method is combined with a staggered time integration solver, including the explicit central difference scheme and the forward-difference strategy, to find the stable solution for the displacement and phase field variables, respectively. The selected time step is smaller than the critical time step prescribed by the Courant-Friedrichs-Lewy condition [18, 93]. A novel stress update procedure is also proposed to simulate the localized failure phenomena.

3.1 Spatiotemporal-discrete scheme

We consider the following interpolations for the displacement and phase-field variables at any point $\boldsymbol{x}$ in the element domain

$$\boldsymbol{u}(\boldsymbol{x}, t) = \sum_{I=1}^{N} \boldsymbol{N}^{\boldsymbol{u}}_I(\boldsymbol{x}) \boldsymbol{u}_I(t) \,, \qquad d(\boldsymbol{x}, t) = \sum_{I=1}^{N} \boldsymbol{N}^{d}_I(\boldsymbol{x}) d_I(t) \,, \tag{51}$$

where $\boldsymbol{u}_I$ and d_I are nodal displacement and phase-field variables at the Ith node, respectively; N is the total number of nodes in each element; and $\boldsymbol{N}^{\boldsymbol{u}}_I$ and $\boldsymbol{N}^{d}_I(\boldsymbol{x})$ are the standard first-order finite element shape functions for the displacement and phase-field.

Moreover, the strain vector in Voigt form and the gradient of the phase-field variable are calculated as

$$\boldsymbol{\varepsilon}\left(\boldsymbol{x}, t\right) = \sum_{I=1}^{N} \boldsymbol{B}^{\boldsymbol{u}}_I(\boldsymbol{x}) \boldsymbol{u}_I(t) \,, \qquad \nabla d\left(\boldsymbol{x}, t\right) = \sum_{I=1}^{N} \boldsymbol{B}^{d}_I(\boldsymbol{x}) d_I(t) \,, \tag{52}$$

where $\boldsymbol{B}^{\boldsymbol{u}}_I$ and $\boldsymbol{B}^{d}_I$ represent the derivative matrices of shape functions for the displacement fields $\boldsymbol{u}$ and the phase-field d.

The spatiotemporal discrete equations for the dynamic equations of equilibrium and the phase-field evolution can be obtained from the standard Galerkin approximation.

$$\boldsymbol{M}\ddot{\mathbf{u}} = \boldsymbol{F}_{\text{ext}}\left(\boldsymbol{u}\right) - \boldsymbol{F}_{\text{int}}\left(\boldsymbol{u}, d\right) \,, \tag{53}$$

$$\boldsymbol{C}\dot{d} = \left\langle \boldsymbol{Y}\left(d, \nabla d, \mathcal{H}^{\text{eq}}\left(\boldsymbol{\varepsilon}, \boldsymbol{\varepsilon}^p, \boldsymbol{\alpha}, d\right)\right)\right\rangle_+ \,. \tag{54}$$

Explicit expressions for the matrices are as follows:

- Mass matrix:

$$\boldsymbol{M} = \bigwedge_{e=1}^{N_e} \int_{\mathcal{B}^e} \boldsymbol{N}_e^{\boldsymbol{u}T} \rho \boldsymbol{N}_e^{\boldsymbol{u}} \mathrm{d}\mathcal{B}^e \,, \tag{55}$$

  where N_e is the number of elements in the computational domain and $\bigwedge_{e=1}^{N_e}$ is the assembly operator.
- Damping matrix:

$$\boldsymbol{C} = \bigwedge_{e=1}^{N_e} \int_{\mathcal{B}^e} \boldsymbol{N}_e^{dT} \eta \boldsymbol{N}_e^{d} \mathrm{d}\mathcal{B}^e \,. \tag{56}$$

- External force matrix:

$$\boldsymbol{F}_{\text{ext}}\left(\boldsymbol{u}\right) = \bigwedge_{e=1}^{N_e} \int_{\mathcal{B}^e} \boldsymbol{N}_e^{\boldsymbol{u}T} \boldsymbol{b} \, \mathrm{d}\mathcal{B}^e + \bigwedge_{e=1}^{N_e^{\boldsymbol{t}}} \int_{\mathit{\Gamma}_{\boldsymbol{t}}^e} \boldsymbol{N}_e^{\boldsymbol{u}T} \bar{\boldsymbol{t}} \, \mathrm{d}\mathit{\Gamma}^e \,, \tag{57}$$

  where $N_e^{\boldsymbol{t}}$ is the number of elements where prescribed tractions are applied, and $\mathit{\Gamma}_{\boldsymbol{t}}^e$ denotes the prescribed traction boundary in the e-th element.
- Internal force matrix:

$$\begin{aligned} \boldsymbol{F}_{\text{int}}\left(\boldsymbol{u}, d\right) = \bigwedge_{e=1}^{N_e} \int_{\mathcal{B}^e} & \Big[g_1\left(d, r\right) \boldsymbol{B}_e^{\boldsymbol{u}T} \mathbb{C} \left(\boldsymbol{\varepsilon}_{\text{vol}}^{e+} + \boldsymbol{\varepsilon}_{\text{dev}}^{e} \right) \\ & + g_1\left(d, r\right) \theta \boldsymbol{B}_e^{\boldsymbol{u}T} \mathbb{C}_{\text{vol}} \boldsymbol{\varepsilon}_{\text{vol}}^{e-} + \left(1 - \theta\right) \boldsymbol{B}_e^{\boldsymbol{u}T} \mathbb{C}_{\text{vol}} \boldsymbol{\varepsilon}_{\text{vol}}^{e-} \Big] \, \mathrm{d}\mathcal{B}^e \,, \end{aligned} \tag{58}$$

  where $\mathbb{C}$ is the stress-strain matrix, which can be decomposed into volumetric and deviatoric parts, i.e., $\mathbb{C}_{\text{vol}}$ and $\mathbb{C}_{\text{dev}}$.
- Coupled plastic-failure dissipation matrix:

$$\begin{aligned} \boldsymbol{Y}\left(d, \nabla d, \mathcal{H}^{\text{eq}}\right) = & \bigwedge_{e=1}^{N_e} \int_{\mathcal{B}^e} \left[\left(1 - d\right) \frac{2}{\mathcal{G}_c} \left[r \left(\mathcal{H}_{vol}^{e+} + \mathcal{H}_{\text{dev}}^{e} \right) + \left(\mathcal{H}_{\text{vol}}^{p+} + \mathcal{H}_{\text{dev}}^{p} \right) \right] \boldsymbol{N}_e^{dT} \right] \mathrm{d}\mathcal{B}^e \\ & - \bigwedge_{e=1}^{N_e} \int_{\mathcal{B}^e} \left[\boldsymbol{N}_e^{dT} d - \ell \mathcal{G}_B \boldsymbol{B}_e^{dT} \nabla d \right] \mathrm{d}\mathcal{B}^e \end{aligned} \tag{59}$$

For the staggered solver, the displacement fields are computed using the explicit central-difference integration scheme, while the phase-field evolution is computed using the explicit forward-difference time-integration strategy.

3.2 Stress updated procedure

Within the time interval $[t_n, t_{n+1}]$, we assume that the known variables are $\boldsymbol{\varepsilon}_{\mathrm{tot},n}$, $\boldsymbol{\varepsilon}_n^e$, $\boldsymbol{\varepsilon}_n^p$, d_n, r_n. We can then calculate the trial volumetric strain tensor $\boldsymbol{\varepsilon}_{\mathrm{vol},n+1}^{\mathrm{trial}}$ and the trial deviatoric strain tensor $\boldsymbol{\varepsilon}_{\mathrm{dev},n+1}^{\mathrm{trial}}$. The stress updated procedure can be summarized as follows.

The volumetric and deviatoric parts of the elastic trial total stress tensor $\boldsymbol{\sigma}_{\mathrm{tot},n+1}^{\mathrm{trial}}$ can be **first** computed as follows

$$\boldsymbol{\sigma}_{\mathrm{vol},n+1}^{\mathrm{trial}} = \mathrm{g}_1\left(d_n, r_n\right)\theta\mathbb{C}_{\mathrm{vol}} : \left(\boldsymbol{\varepsilon}_{\mathrm{tot},n+1}^{\mathrm{trial}} - \boldsymbol{\varepsilon}_n^p\right) + \left(1-\theta\right)\mathbb{C}_{\mathrm{vol}} : \left(\boldsymbol{\varepsilon}_{\mathrm{tot},n+1}^{\mathrm{trial}} - \boldsymbol{\varepsilon}_n^p\right) \tag{60a}$$

$$\boldsymbol{\sigma}_{\mathrm{dev},n+1}^{\mathrm{trial}} = \mathrm{g}_1\left(d_n, r_n\right)\mathbb{C}_{\mathrm{dev}} : \left(\boldsymbol{\varepsilon}_{\mathrm{tot},n+1}^{\mathrm{trial}} - \boldsymbol{\varepsilon}_n^p\right) \tag{60b}$$

Then, the equivalent stress at $t = n+1$ is computed as

$$Q_{n+1}^{\mathrm{trial}} = \sqrt{\frac{3}{2}\left(\boldsymbol{\sigma}_{\mathrm{dev},n+1}^{\mathrm{trial}}\right) : \left(\boldsymbol{\sigma}_{\mathrm{dev},n+1}^{\mathrm{trial}}\right)} \tag{61}$$

Next, the discrete trial yielding condition is given by

$$\mathcal{F}_{n+1}^{\mathrm{trial}}\left(\pi_{n+1}^{\mathrm{trial}}, Q_{n+1}^{\mathrm{trial}}\right) = \sqrt{\frac{\left(\pi_{n+1}^{\mathrm{trial}}\right)^2}{A_{n+1}^2} + \frac{\left(Q_{n+1}^{\mathrm{trial}}\right)^2}{B_{n+1}^2}} - 1 \leq 0 \tag{62}$$

where A_{n+1} and B_{n+1} are the yielding shape coefficients at $t = n+1$, which are

$$A_{n+1} = \left(1-\gamma\right)P_{n+1}^{\mathrm{trial}} + \frac{1}{2}\gamma P_c \tag{63a}$$

$$B_{n+1} = \mu\left[\left(1-\alpha\right)P_{n+1}^{\mathrm{trial}} + \frac{1}{2}\alpha\gamma P_c\right] \tag{63b}$$

Then, considering the Kuhn-Tucker conditions,

$$\Delta\lambda \geq 0, \qquad \mathcal{F}\left(\boldsymbol{\sigma}_{\mathrm{vol},n+1}^{\mathrm{trial}}, \boldsymbol{\sigma}_{\mathrm{dev},n+1}^{\mathrm{trial}}\right) \leq 0, \qquad \Delta\lambda\mathcal{F}\left(\boldsymbol{\sigma}_{\mathrm{vol},n+1}^{\mathrm{trial}}, \boldsymbol{\sigma}_{\mathrm{dev},n+1}^{\mathrm{trial}}\right) = 0 \tag{64}$$

the classical elastic predictor and plastic corrector, i.e., the return-mapping algorithm, is adopted to solve the elastoplastic solutions.

If $\mathcal{F}_{n+1}^{\mathrm{trial}} \leq 0$, the trial total stress tensor $\boldsymbol{\sigma}_{\mathrm{tot},n+1}^{\mathrm{trial}} = \boldsymbol{\sigma}_{\mathrm{vol},n+1}^{\mathrm{trial}} + \boldsymbol{\sigma}_{\mathrm{dev},n+1}^{\mathrm{trial}}$ is located in the elastic deformation regime, which indicates $\boldsymbol{\sigma}_{\mathrm{tot},n+1} = \boldsymbol{\sigma}_{\mathrm{tot},n+1}^{\mathrm{trial}}$. On the other hand, if $\mathcal{F}_{n+1}^{\mathrm{trial}} \geq 0$, the trial total stress tensor is not admissible, and the return-mapping algorithm is needed as a plastic corrector step.

The computational schematic of the volumetric and deviatoric stress components in the return mapping algorithm is depicted in Figure 3. Using the plastic flow rule of Eqs. 47a and 47b, the volumetric and deviatoric plastic strain increments **then** read

$$\Delta\boldsymbol{\varepsilon}^p_{\mathrm{vol}} = \frac{\langle \mathcal{F}^{\mathrm{trial}}_{n+1} \rangle}{\eta \left(1 + \mathcal{F}^{\mathrm{trial}}_{n+1}\right)} \frac{\pi_{n+1}}{A^2_{n+1}} \cdot \boldsymbol{N}_{\mathrm{v}}\,, \tag{65}$$

$$\Delta\boldsymbol{\varepsilon}^p_{\mathrm{dev}} = \frac{\langle \mathcal{F}^{\mathrm{trial}}_{n+1} \rangle}{\eta \left(1 + \mathcal{F}^{\mathrm{trial}}_{n+1}\right)} \frac{Q_{n+1}}{B^2_{n+1}} \cdot \boldsymbol{N}_{\mathrm{d}}\,, \tag{66}$$

where

$$\boldsymbol{N}_d = \sqrt{\frac{3}{2}} \frac{\boldsymbol{\sigma}^{\mathrm{trial}}_{\mathrm{dev},n+1}}{\|Q^{\mathrm{trial}}_{n+1}\|} \tag{67}$$

and the following updated stress states $\boldsymbol{\sigma}_{\mathrm{vol},n+1}$ and $\boldsymbol{\sigma}_{\mathrm{dev},n+1}$ read

$$\begin{aligned} \boldsymbol{\sigma}_{\mathrm{vol},n+1} &= \boldsymbol{\sigma}^{\mathrm{trial}}_{\mathrm{vol},n+1} - \Delta\sigma^P \boldsymbol{N}_{\mathrm{v}} \\ &= \boldsymbol{\sigma}^{\mathrm{trial}}_{\mathrm{vol},n+1} - \mathrm{g}_1\left(d_n, r_{n+1}\right) \theta \mathbb{C}_{\mathrm{vol}} : \Delta\boldsymbol{\varepsilon}^p_{\mathrm{vol}} - \left(1-\theta\right) \mathbb{C}_{\mathrm{vol}} : \Delta\boldsymbol{\varepsilon}^p_{\mathrm{vol}} \end{aligned} \tag{68}$$

$$\boldsymbol{\sigma}_{\mathrm{dev},n+1} = \boldsymbol{\sigma}^{\mathrm{trial}}_{\mathrm{dev},n+1} - \Delta\sigma^Q \boldsymbol{N}_{\mathrm{d}} = \boldsymbol{\sigma}^{\mathrm{trial}}_{\mathrm{dev},n+1} - \mathrm{g}_1\left(d_n, r_{n+1}\right) \mathbb{C}_{\mathrm{dev}} : \Delta\boldsymbol{\varepsilon}^p_{\mathrm{dev}} \tag{69}$$

where

$$r_{n+1} = r_n + \frac{\Delta\boldsymbol{\varepsilon}^p_{\mathrm{eq},n+1}}{\varepsilon^p_{\mathrm{eq,\ crit}}} \tag{70}$$

in which

$$\Delta\boldsymbol{\varepsilon}^p_{\mathrm{eq},n+1} = \sqrt{\frac{2}{3} \Delta\boldsymbol{\varepsilon}^p_{\mathrm{dev}} : \Delta\boldsymbol{\varepsilon}^p_{\mathrm{dev}}}\,. \tag{71}$$

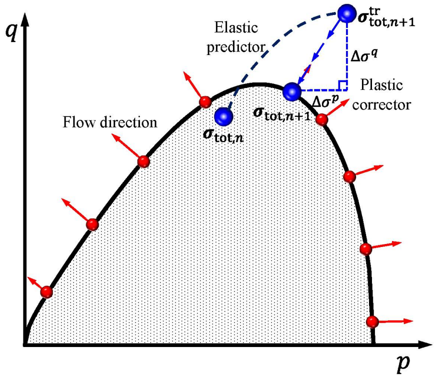

Fig. 3. Schematics of flow directions at different confining pressures (indicated by the red arrow) and the general return mapping geometric interpretation.

4 Benchmark problems

To validate our model, we consider the notched Bentheim sandstone specimens tested in triaxial compression by Vajdova and Wong [110] and Tembe et al. [107]. The laboratory specimens had a diameter of 18.4 mm and a height of 38.1 mm. For purposes of analysis, we simulated these tests in plane strain with the geometric configuration shown in Figure 4(a) and the finite element mesh shown in Figure 4(b). The V-shaped notches in the numerical model are 2 mm × 2 mm, as shown in Figure 4(c), resulting in an inner width of $18.4 - 2 \times 2.0 = 14.4$ mm for the numerical model. A total of 8,776 triangular elements were used in the finite element mesh with $h_{\max} = 0.4$ mm.

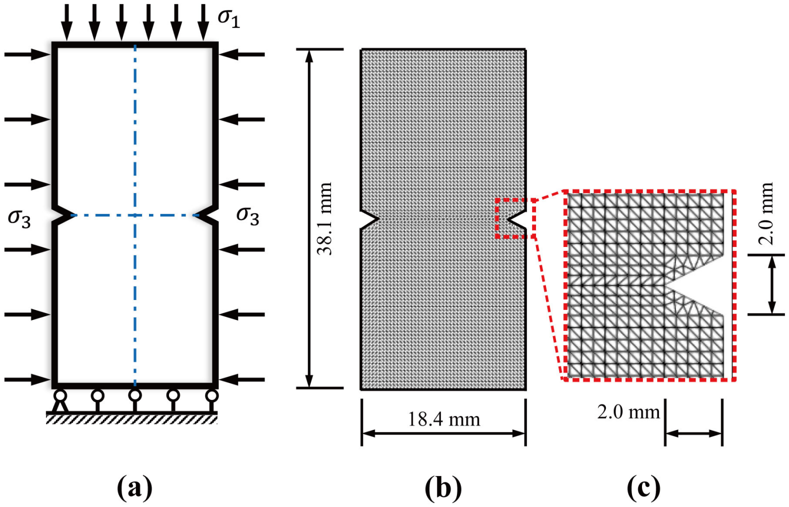

Fig. 4. Plane strain compression of notched Bentheim sandstone sample: (a) schematic diagram, (b) mesh discretization and (c) enlarged zone of V-shape notches.

Based on the literature [64, 107, 108], the following material parameters were used in the simulations: mass density $\rho = 2,450$ kg/m^3, Young's modulus $E = 19.2$ GPa, Poisson's ratio $\nu = 0.268$, critical fracture energy release rate $\mathcal{G}_c = 1.0$ J/m^2, viscosity coefficient $\zeta = 0.1$, plastic viscosity $\eta = 5.0 \times 10^{-3}$ Pa^{-1}·s, plastic compressibility $\Lambda_c = 1.5 \times 10^{-3}$, and crushing potential $\theta = 0.1$. Also based on the literature [13, 64, 67], the following parameters for the plasticity model were assumed: $P_c^0 = 420.0$ MPa, $\varepsilon^p_{\text{eq, crit}} = 0.1$, $\mu = 1.5$, $\alpha = 0.5$ and $\gamma = 1.0$. The computational time step was $\Delta t = 1.0 \times 10^{-7}$ s and the length scale parameter was $\ell = 0.6$ mm.

The simulations consisted of first applying a confining pressure of 250 MPa followed by an axial load of 2 μm/s, emulating the loading sequence in the experiments. The calculated vertical displacement u_2 and phase-field variable

d are displayed in Figures 5(a) and (b). We observe that the compaction band first initiates at the tip of the two V-shape notches and propagates horizontally toward the center. The result is a thin compaction band oriented perpendicular to the major compressive stress, as shown in Figure 5.

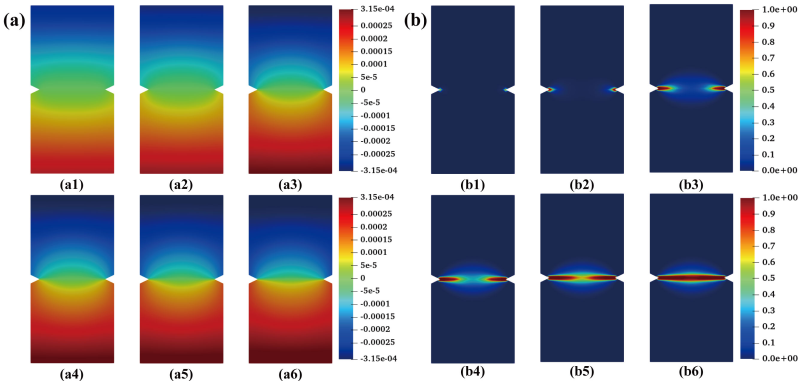

Fig. 5. Numerical results of compaction bands formation in the notched Bentheim sandstone sample: (a) vertical displacement field (unit: m), and (b) compaction band formation.

Figure 6 compares the stress-strain curve for the simulated Bentheim sandstone sample with the quasi-static simulation of Ip and Borja [64]. Both simulations employed a plane strain assumption, so the comparison is meaningful. Six representative points corresponding to the snapshots shown in Figure 5 are labeled in the stress-strain curve shown in Figure 6. Both simulations predicted an initially hardening response with comparable peak strengths. However, substantial softening is observed in the current simulation. Compared with the simulation of Ip and Borja, the current simulation predicts a more pronounced re-hardening response after the compaction band has formed, similar to that observed in the laboratory experiments [107, 108]. Because the laboratory experiments were conducted in triaxial condition whereas the two simulations were conducted in plane strain condition, the experimental curve was not superimposed in Figure 6.

Remark. Like the formulation by Ip and Borja [64], the onset of a compaction band in the present work is determined by the critical energy release rate $\mathcal{G}_c$ and not by a softening behavior. There is no bifurcation analysis needed in either work, so it is possible to form a compaction band even in the hardening regime.

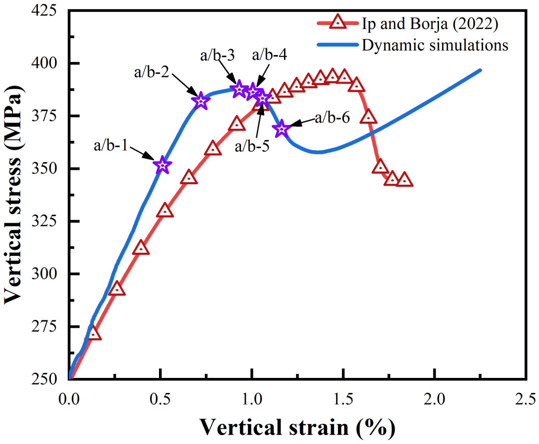

Fig. 6. Comparison of the simulated stress-strain response with the simulation result of Ip and Borja [64] for the Bentheim sandstone sample under a confining pressure of 250 MPa.

Figure 7 plots the equivalent plastic strain $\varepsilon^p_{\mathrm{eq}}$ and volumetric plastic strain $\varepsilon^p_{\mathrm{vol}}$ at three representative simulations stages. Qualitatively, we observe that the volumetric plastic deformation dominates the compaction band formation, with the volumetric plastic strain being much more intense.

Figure 8 plots the initial yield stress predicted by the phase-field simulation on the deviatoric stress versus mean normal stress plane against the experimental data reported by Vajdova and Wong [110] and the results of a theoretical analysis conducted by Tembe et al. [107] employing linear elastic fracture mechanics (LEFM). The initial yield stress predicted by the phase-field simulation lies within the region defined by the experimental and theoretical curves. In addition, the inset in Figure 8 also indicates that the failure initiation pattern during compaction band formation agrees well with both macroscopic and microscopic observations [107, 110].

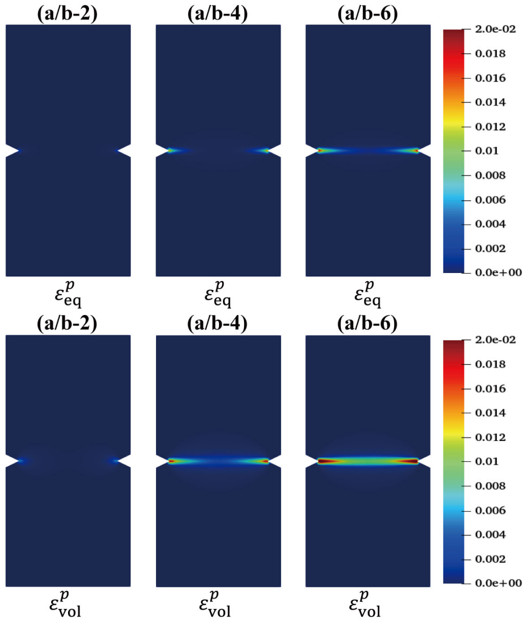

Fig. 7. Equivalent plastic strain $\varepsilon^p_{\mathrm{eq}}$ (top row) and volumetric plastic strain $\varepsilon^p_{\mathrm{vol}}$ (bottom row) during the formation of a compaction band.

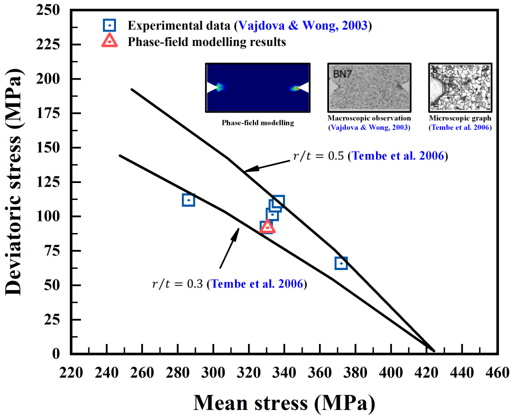

Fig. 8. Initial yield stress for the notched Bentheim sandstone samples obtained from the phase-field simulation, laboratory tests [107, 110] and LEFM theoretical analysis [107].

A comparison of ultimate failure patterns obtained from the phase-field simulation, laboratory experiment [107], and breakage mechanics modeling [43] is depicted in Figure 9. This result was obtained after conducting mesh convergence studies with $h_{\max} = 0.2, 0.3, 0.4$, and 0.6 mm, and with the same characteristic length scale of $\ell = 0.6$ mm, which produced nearly identical solutions. Both the breakage mechanics and phase-field simulation results compare well with the experimental observations. However, we shall show in subsequent simulations that the proposed phase-field model can capture not only the main compaction band straight form but also the shear-enhanced and secondary deformation bands that form away from the mid-section.

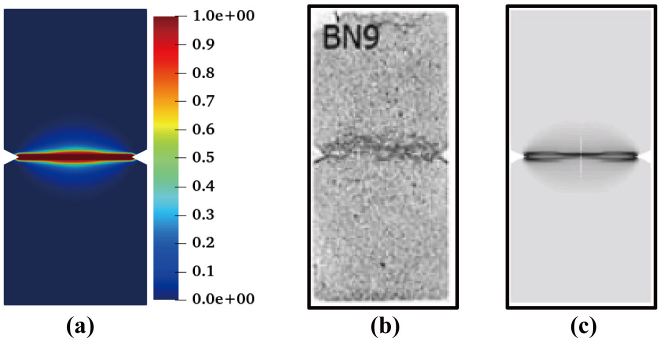

Fig. 9. Comparison of compaction bands in the notched Bentheim sandstone sample obtained from: (a) phase-field simulation, (b) experimental observation [107], and (c) breakage mechanics modeling [43].

The grain crushing potential θ was introduced by Ip and Borja [64] to limit the degradation of the elastic stiffness due to grain crushing during the formation of a compaction band. To investigate its impact on the phase-field simulations, four V-shape notched Bentheim sandstone samples were subjected to plane strain compression under a confining pressure of $\sigma_3 = 300.0$ MPa. The resulting localization patterns and mechanical responses are plotted in Figures 10(a) and 10(b), respectively. It can be observed that θ has only a slight effect on the ultimate compaction band formed (Figure 10a) but has a more pronounced effect on the softening responses as the compaction bands propagate (Figure 10b).

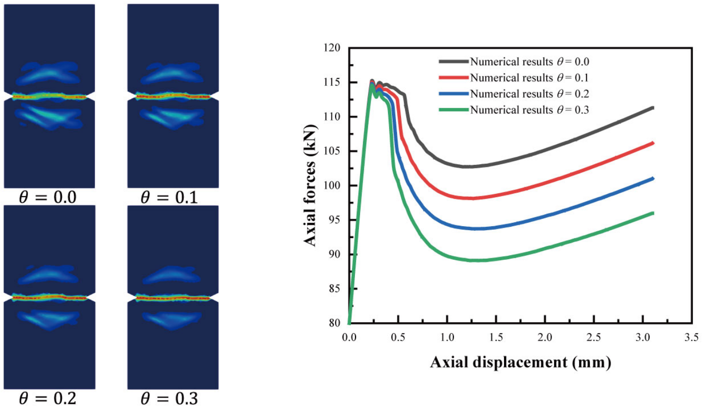

(a) **(b)**

Fig. 10. Effect of the grain crushing potential θ on: (a) compaction band patterns; and (b) mechanical responses.

In all four simulations, we also note from Figure 10(a) that although the main compaction bands are straight and thin, they are surrounded by secondary chevron bands delineated by the light-blue regions. A similar deformation feature has been reported in the literature using viscoplastic constitutive modelling of compaction creep tests in porous rocks [96, 97]. This intriguing deformation style has not been reproduced in the quasi-static simulations of compaction band formation [64]. This could point to the role of dynamic effects on the ensuing style of deformation bands observed in the field. Other factors that could impact the geometric style of compaction bands include the boundary conditions [97], heterogeneous distribution of porosity [15], rock anisotropy [98], fluid flow [125, 126], partial saturation [63, 65], and chemical reaction [27].

5 Numerical simulations

We also conducted a series of hypothetical numerical simulations on Bentheim sandstone samples to further demonstrate the capability and performance of the phase-field model. All simulations were conducted under 2D plane strain condition on a rectangular sample having a width of 50 mm and a height of 100 mm, see Figure 11. The sample was first subjected to a confining stress and then loaded in the vertical direction by prescribing a vertical displacement on the top boundary at the rate of 2.0×10^{-3} m/s while holding the bottom boundary fixed along the vertical direction, see Figure 11(a). To trigger strain localization, we recognize that rock samples are inherently heterogeneous even at the smaller scale [17, 95], so a weak element was introduced at the center of the sample by setting an initial value of $d = 0.05$ for the phase-field variable, see Figures 11(b) and 11(c).

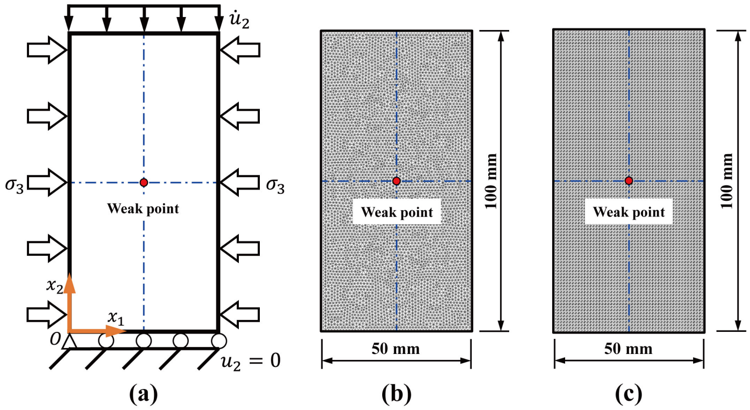

Fig. 11. Problem domain and boundaries: (a) geometry and boundary conditions; (b) unstructured mesh and (c) structured mesh.

Referring to Jacquey and Regenauer-Lieb [68], we assumed the following values of material parameters in the numerical simulations: mass density $\rho = 2,450$ kg/m^3, Young's modulus $E = 22.3$ GPa, Poisson's ratio $\nu = 0.17$, critical fracture energy release rate $\mathcal{G}_c = 1.0$ J/m^2, viscosity coefficient $\zeta = 0.1$, plastic viscosity $\eta = 5.0 \times 10^{-3}$ Pa$^{-1} \cdot$ s, and plastic compressibility $\Lambda_c = 2.0 \times 10^{-3}$. Initial values of the plastic variables are assumed as: $P_c^0 = 20$ MPa, $\varepsilon^p_{\text{eq, crit}} = 0.1$, $\mu = 1.2$, $\alpha = 0.65$ and $\gamma = 0.8$. In the present numerical simulations, the computational time step and the internal characteristic length were taken as $\Delta t = 1.0 \times 10^{-7}$ s and $\ell = 8$ mm, respectively.

5.1 Mesh sensitivity and convergence studies

To demonstrate the robustness of our approach, we study mesh sensitivity and numerical convergence on dynamic strain localization. Two numerical samples with the irregular and regular FE meshes (see Figure 11b and Figure 11c) are simulated in 2D plane strain compression tests with $\sigma_3 = 60$ MPa. The comparisons of localized failure patterns and mechanical responses are plotted in Figure 12(a) and Figure 12(b), respectively. Figure 12 shows that the location, orientation, and thickness of compaction bands obtained from the two models are approximately the same. The mechanical responses of $Q \sim \varepsilon_a$ curves in two numerical tests are also similar, which demonstrate the mesh independence and low mesh sensitivity of our model.

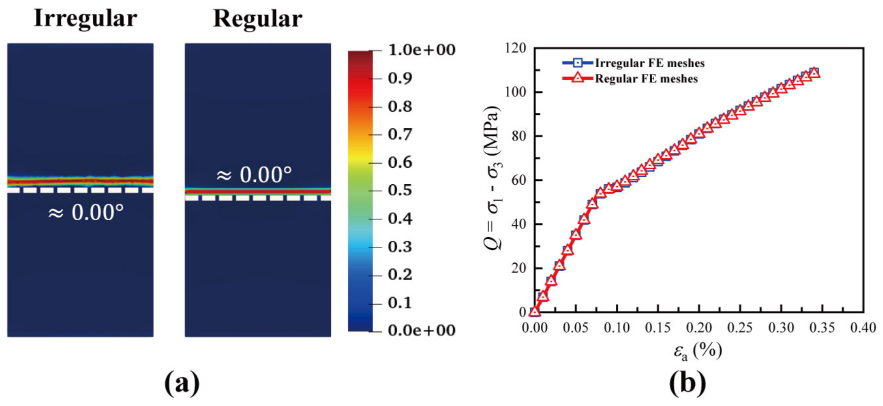

Fig. 12. Effect of mesh discretization on (a) localized failure patterns and (b) $Q \sim \varepsilon_a$ curves of two Bentheim sandstone samples in 2D plane strain compression tests with $\sigma_3 = 60$ MPa.

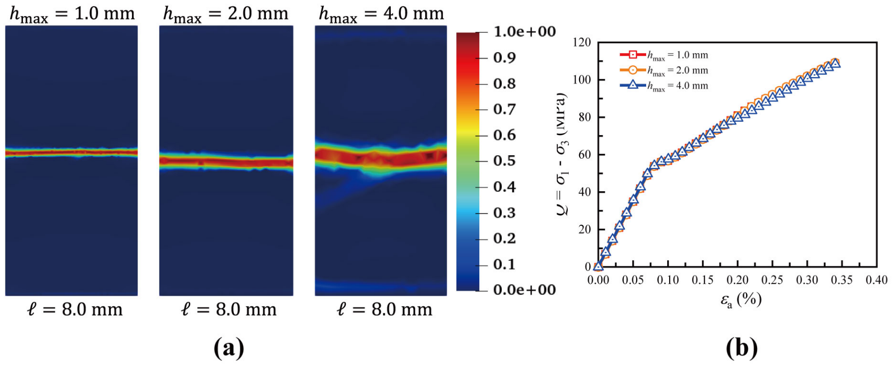

Fig. 13. Effect of $\ell / h_{\max}$ on dynamic strain localization in the numerical tests with the fixed $\ell = 8$ mm: (a) localized failure patterns and (b) $Q \sim \varepsilon_a$ curves.

To study the numerical convergence of finite element solutions, we focus on two kinds of numerical samples: (i) samples with different $h_{\max}$ and a fixed ℓ, and (ii) samples with different ℓ's and a fixed $h_{\max}$. The confining pressures in 2D plane strain tests are kept as $\sigma_3 = 60$ MPa. For the fixed $\ell = 8$ mm, the localized deformation bands and mechanical responses of three numerical samples are plotted in Figure 13(a) and Figure 13(b), respectively. The location and orientation of pure compaction bands in three Bentheim sandstone samples are close to each other. The numerical predictions of mechanical responses, i.e., $Q \sim \varepsilon_a$ curves, in three samples are also similar, while we observe from Figure 13 that the thickness of pure compaction bands increases as the ratio of $\ell/h_{\max}$ decreases.

For the fixed $h_{\max} = 1$ mm, the localized failure patterns and the relevant $Q \sim \varepsilon_a$ curves in three numerical samples with various ℓ's are compared in Figure 14(a) and Figure 14(b), respectively. When $h_{\max}$ is fixed at 1 mm, we observe that $\ell/h_{\max}$ has slight effects on the predicted compaction bands. The above comparisons further demonstrate the numerical convergence and mesh independence of our new phase-field approach for modeling dynamic strain localization.

For the fixed $h_{\max} = 1$ mm, the localized failure patterns and the relevant $Q \sim \varepsilon_a$ curves in three numerical samples with various ℓ's are compared in Figure 14(a) and Figure 14(b), respectively. When $h_{\max}$ is fixed at 1 mm, we observe that $\ell/h_{\max}$ has slight effects on the predicted compaction bands. The above comparisons further demonstrate the numerical convergence and mesh independence of our new phase-field approach for modeling dynamic strain localization.

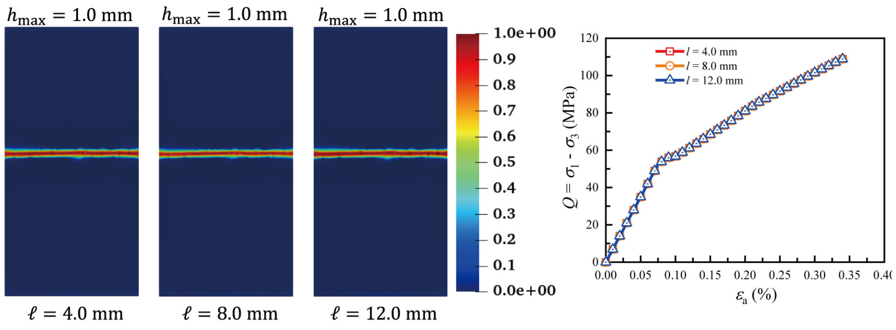

(a) **(b)**

Fig. 14. Effect of $\ell/h_{\max}$ on dynamic strain localization in the numerical tests with a fixed $h_{\max} = 1$ mm: (a) localized failure patterns and (b) $Q \sim \varepsilon_a$ curves.

5.2 Dynamic strain localization process

To further study the dynamic strain localization process, we look more closely into the spatiotemporal localization and mechanical responses of the Bentheim sandstone sample in plane strain compression simulated with $\sigma_3 = 60$ MPa. Figures 15(a)-(d) show the spatiotemporal distributions of d, u_2, $\varepsilon^p_{\mathrm{eq}}$ and $\varepsilon^p_{\mathrm{vol}}$, respectively. During the formation of the localized deformation band, we consider eight representative snapshots in Figures 15(a)-(d) and denote them in the $\sigma_1 \sim \varepsilon_1$ curve shown in Figure 16(a), and in the $\varepsilon_{\mathrm{vol}} \sim \varepsilon_1$ curve shown in Figure 16(b). From Figure 15(a)-(d), we observe that the concentration of accumulative equivalent and volumetric plastic strains drive the initiation and propagation of compaction bands with a maximum value of $d = 0.01$. The evolution of compaction bands is represented by snapshots I $\sim$ IV in Figures 16(a) and 16(b). The enlarged zones in $\sigma_1 \sim \varepsilon_1$ and $\varepsilon_{\text{vol}} \sim \varepsilon_1$ curves indicate that the slight strain-hardening phenomena occurs during the formation of compaction bands. When the deviatoric loads increase, the dynamic strain localization at macro-scale is initiated around the weak point, and propagates towards lateral boundaries normal to the axial direction. The formation of compaction bands is accompanied with the recognizable strain-hardening process in the $\sigma_1 \sim \varepsilon_1$ and $\varepsilon_{\text{vol}} \sim \varepsilon_1$ curves, as shown in Figures 16. Furthermore, when comparing the spatiotemporal distributions of $\varepsilon^p_{\text{eq}}$ and $\varepsilon^p_{\text{vol}}$, we find that the volumetric plastic strain in compression dominates the dynamic strain localization process.

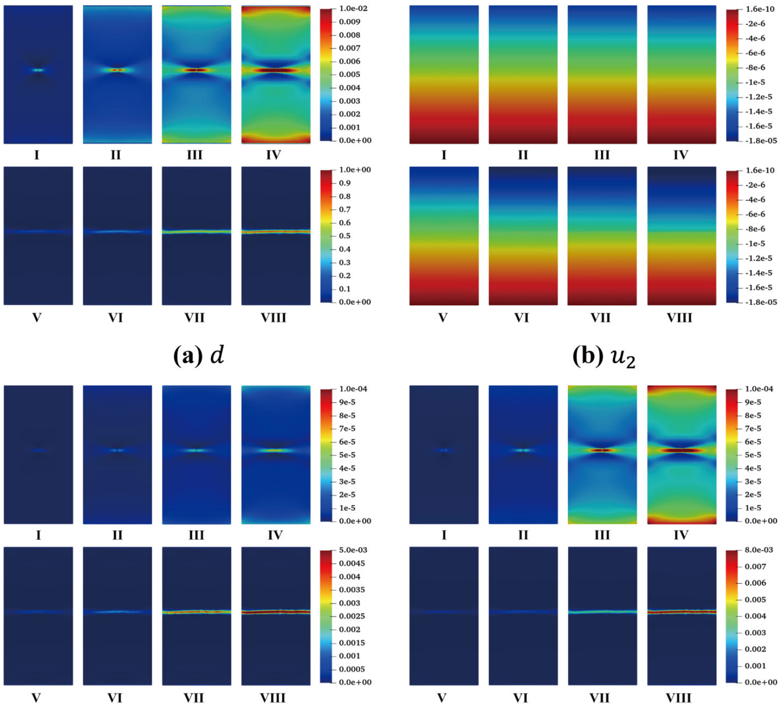

(a) d (b) u_2

(c) $\varepsilon^p_{\text{eq}}$ (d) $\varepsilon^p_{\text{vol}}$

Fig. 15. Dynamic strain localization process at $\sigma_3 = 60$ MPa: Snapshots of spatiotemporal distributions of (a) phase-field variable, (b) vertical displacement, (c) equivalent plastic strain, and (d) volumetric plastic strain.

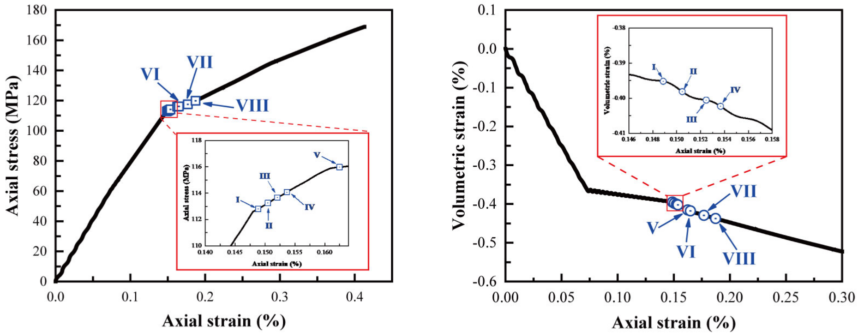

(a) (b)

Fig. 16. Mechanical responses of dynamic strain localization process at $\sigma_3 = 60$ MPa: (a) axial stress versus axial strain, and (b) volumetric strain versus axial strain.

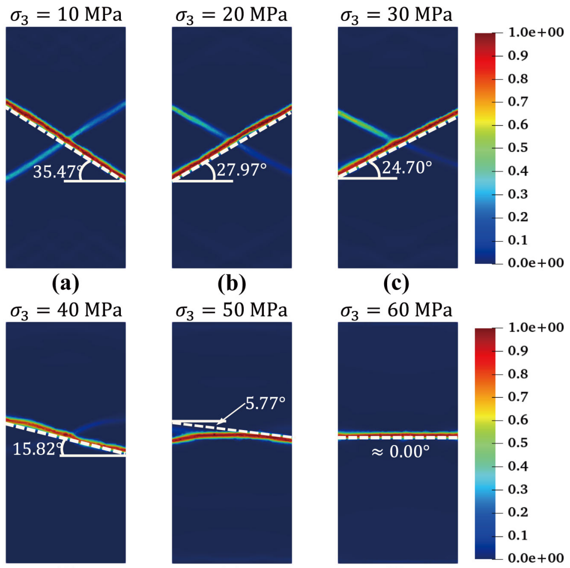

(d) (e) (f)

Fig. 17. Effect of σ_3 on the localized deformation band patterns in the plane strain compression tests.

5.3 Effect of confining pressure

To investigate the effect of confining pressure on the dynamic strain localization and mechanical responses, we simulate six intact Bentheim sandstone samples in plane strain compression with different σ_3. The confining pressure σ_3 is changed from 10 MPa to 60 MPa in increments of 10 MPa. Figure 17 shows the resulting localized deformation band patterns, suggesting that the confining pressure plays a critical role in the dynamic strain localization. Based on the ratio $\varepsilon^p_{\mathrm{eq}}/\varepsilon^p_{\mathrm{vol}}$, dilation shear bands, shear-enhanced compaction bands, and pure compaction bands can be recognized. When σ_3 is increased from 10 MPa to 60 MPa, the localized deformation band pattern first changes from a dilation shear band with a high orientation angle (Figures 17 a-b) to a shear-enhanced compaction band with a medium inclination angle (Figures 17 c-d), to a pure compaction band with a low inclination angle (Figures 17 e-f). The slightly curved shape of shear-enhanced compaction bands is caused by the combined compressive normal and shear stresses. These results indicate that our model can capture the transition from dilatant to compactive strain localization, which agrees with results from breakage mechanics theory [38].

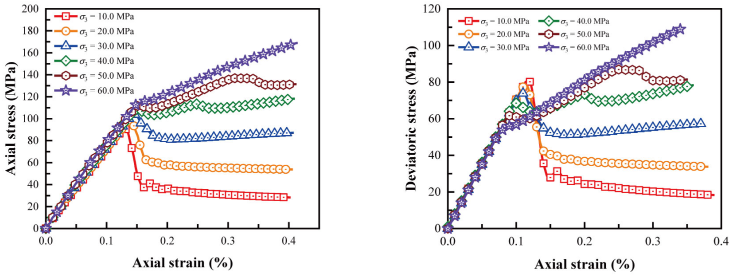

(a) **(b)**

Fig. 18. Effect of σ_3 on (a) $\sigma_1 \sim \varepsilon_1$ and (b) $Q \sim \varepsilon_1$ curves for Bentheim sandstone specimens in the plane-strain compression tests.

Figure 18(a) shows the relevant macro-mechanical axial stress versus axial strain curves for these six simulations. Figure 18(b) shows the deviatoric stress $Q = \sigma_1 - \sigma_3$ versus axial strain ε_a at different confining pressures. We observe from Figure 18(a) that the peak axial stress increases as σ_3 increases, while Figure 18(b) shows that the peak deviatoric stress decreases as σ_3 increases.

At low confining pressures (10 and 20 MPa), the samples attain a peak stress beyond which strain softening occurs with a significant stress drop during the dilation shear band formation. At medium confining pressures (30 and 40 MPa), shear-enhanced compaction bands initiate and propagate, accompanied by a slight stress drop at the post-failure stage. At high confining pressures (50 and 60 MPa), a pure compaction band forms with a monotonic strain-hardening response. Figure 19 provide the graphic illustration of the localization patterns over the whole range of loading conditions simulated using our model. The initial yield stress points of samples at low σ_3 are located in the dilatant regime, while the initial yield stress points at high σ_3 reside in the compact regime. Overall, as the confining pressure increases the localized deformation band pattern transforms from a shear band type with significant strain softening, to shear-enhanced compaction band with moderate strain softening, to pure compaction band with pronounced strain hardening.

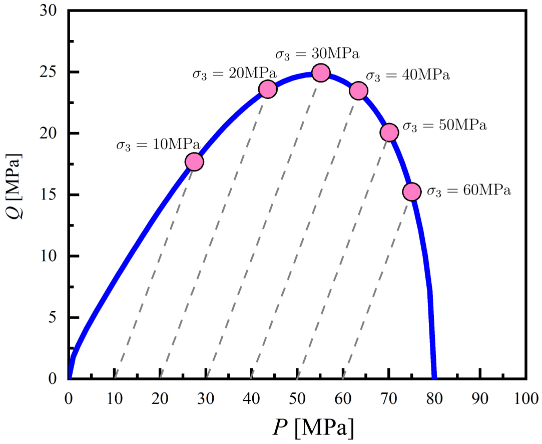

Fig. 19. Graphic illustration of the relation between plane-strain compressive loading paths (i.e., gray dash lines) and initial yield surface (i.e., blue solid curve) during strain localization.

The predicted $\varepsilon_{\text{vol}} \sim \varepsilon_a$ curves are plotted in Figure 20. When the deformation band changes from a shear-band type to a pure compaction band, the minimum value of volumetric strain decreases. At the onset of localized deformation, we observe that the volumetric strain first decreases significantly due to grain crushing. As ε_a increases and the band propagates, ε_{vol} decreases slightly due to pore collapse. At low confining pressures, the sample dilates at the post-failure stage (see Figure 20) due to grain sliding and rearrangement. However, at high confining pressures the sample compacts, indicating that pore collapse and porosity reduction continue during the development of pure compaction bands. All of these observations agree with experimental observations [1, 107].

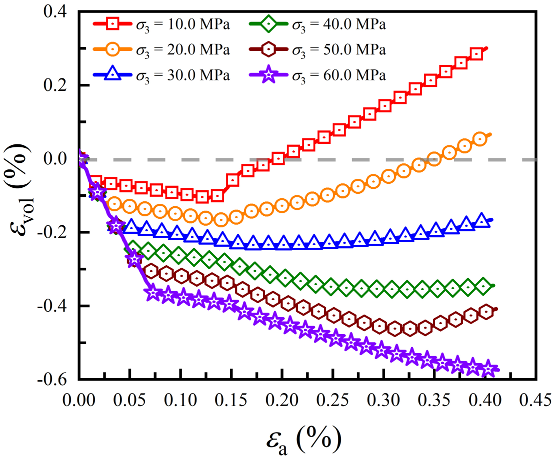

Fig. 20. Effect of σ_3 on $\varepsilon_{\text{vol}} \sim \varepsilon_a$ curves in the plane strain compression tests.

6 Closure

We have simulated the dynamic formation and propagation of compaction bands in high-porosity rocks using the phase-field approach. Main ingredients of the approach include separate degradation mechanisms in compression, dilation, and shear to accommodate for disturbances that propagate in a wave-like fashion; and a staggered numerical time-integration strategy employing the explicit central difference scheme for the displacement field and the forward-difference scheme for the phase-field variable. We have simulated the formation of a compaction band in a V-shape notched Bentheim sandstone sample in plane strain compression and obtained a complex geometric style consisting of a main pure compaction band and secondary double-chevron bands propagating away from the main compaction band. This style of deformation is distinct from the style obtained by Ip and Borja [64] from a similar simulation based on a quasi-static formulation, underscoring the effects of dynamic strain localization on the ensuing geometric style of localized deformation. We have also investigated the effects of confining pressures, mesh discretization, mesh sizes and internal characteristic lengths on the numerically predicted deformation band. A plastic strain-based index is proposed to differentiate between shear bands, shear-enhanced compaction bands, and pure compaction bands. Work is underway to incorporate the effects of anisotropy and creep [26, 74, 94, 127, 128] on the localization of deformation in rocks.

CRediT authorship contribution statement

Yunteng Wang: Conceptualization, Methodology, Software, Validation, Formal analysis, Investigation, Figures, Writing - Original Draft, Review Revision & Editing **Ronaldo I. Borja:** Conceptualization, Methodology, Supervision, Writing - Original Draft, Review Revision & Editing; **Wei Wu:** Conceptualization, Methodology, Supervision, Writing - Original Draft, Review Revision & Editing.

Acknowledgments

The authors wish to acknowledge the financial support from the Austrian Science Fund (FWF) for Lise Meitner Programme **(Grant No. M 3340-N)**, Otto Pregl Foundation of Fundamental Geotechnical Research in Vienna, and EU Horizon 2020 RISE project - FRAMED **(Grant No. 734485)** and EU Horizon 2020 RISE project - HERCULES **(Grant No. 778360)**. The second author acknowledges the support from the US National Science Foundation under **Grant No. CMMI-1914780**. Moreover, author also would like to Ms. Sabrina C.Y. Ip for her helpful discussion and comments.

References

[1] Abdallah Y, Sulem J, Bornert M, Ghabezloo S, Stefanou I (2021). Compaction banding in high-porosity carbonate rocks: 1. Experimental observations. Journal of Geophysical Research: Solid Earth 126(1): e2020JB020538.

[2] Abdallah Y, Sulem J, Stefanou I (2020). Compaction banding in high-porosity carbonate rocks: 2. A gradient-dependent plasticity model. Journal of Geophysical Research: Solid Earth 125(12):e2020JB020610.

[3] Alessi R, Ambati M, Gerasimov T, Vidoli S, Lorenzis LD (2018). Comparison of phase-field models of fracture coupled with plasticity. In: Oñate E, Peric D, de Souza Neto E, Chiumenti M (eds) Advances in Computational Plasticity. Computational Methods in Applied Sciences, Vol 46. Springer, Cham, pp. 1–21.

[4] Ambati M, Gerasimov T, De Lorenzis L (2015). A review on phase-field models of brittle fracture and a new fast hybrid formulation. Computational Mechanics 55(2):383–405.

[5] Ambati M, Gerasimov T, De Lorenzis L (2015). Phase-field modeling of ductile fracture. Computational Mechanics 55(5):1017–1040.

[6] Ambati M, Kruse R, De Lorenzis L (2016). A phase-field model for ductile fracture at finite strains and its experimental verification. Computational Mechanics 57(1):149–167.

[7] Amor H, Marigo J-J, Maurini C (2009). Regularized formulation of the variational brittle fracture with unilateral contact: Numerical experiments. Journal of the Mechanics and Physics of Solids 57(8):1209–1229.

[8] Araujo REB, Bezerra FHR, Nogueira FCC, Balsamo F, Carvalho BRBM, Souza JAB, Sanglard JCD, de Castro DL, Melo ACC (2018). Basement control on fault formation and deformation band damage zone evolution in the Rio do Peixe Basin, Brazil. Tectonophysics 745:117–131.

[9] Arriaga M, Waisman H (2017). Combined stability analysis of phase-field dynamic fracture and shear band localization. International Journal of Plasticity 96:81–119.

[10] Arriaga M, Waisman H (2018). Stability analysis of the phase-field method for fracture with a general degradation function and plasticity induced crack generation. Mechanics of Materials 116:33–48.

[11] Aydin A, Borja RI, Eichhubl P (2006). Geological and mathematical framework for failure modes in granular rock. Journal of Structural Geology 28(1):83–98.

[12] Baud P, Klein E, Wong T-f (2004). Compaction localization in porous sandstones: spatial evolution of damage and acoustic emission activity. Journal of Structural Geology 26(4):603–624.

[13] Baud P, Vajdova V, Wong T-f (2006). Shear-enhanced compaction and strain localization: Inelastic deformation and constitutive modeling of four porous sandstones. Journal of Geophysical Research: Solid Earth 111(B12). https://doi.org/10.1029/2005JB004101

[14] Baud P, Vinciguerra S, David C, Cavallo A, Walker E. Reuschlé T, (2009). Compaction and failure in high porosity carbonates: Mechanical data and microstructural observations. Pure and Applied Geophysics 166(5):869–898.

[15] Baud P, Reuschlé T, Ji Y, Cheung CS, Wong TF (2015). Mechanical compaction and strain localization in Bleurswiller sandstone. Journal of Geophysical Research: Solid Earth 120(9): 6501–6522.

[16] Baud P, Schubnel A, Heap M, Rolland A (2017). Inelastic compaction in high-porosity limestone monitored using acoustic emissions. Journal of Geophysical Research: Solid Earth 122(12):9989–10008.

[17] Bennett KC, Berla AL, Nix WD, Borja RI (2015). Instrumented nanoindentation and 3D mechanistic modeling of a shale at multiple scales. Acta Geotechnica 10(1):1–14.

[18] Borden, M. J., Verhoosel, C. V., Scott, M. A., Hughes, T. J., Landis, C. M. (2012). A phase-field description of dynamic brittle fracture. Computer Methods in Applied Mechanics and Engineering, 217, 77–95.

[19] Borden MJ, Hughes TJR, Landis CM, Anvari A, Lee IJ (2016). A phase-field formulation for fracture in ductile materials: Finite deformation balance law derivation, plastic degradation, and stress triaxiality effects. Computer Methods in Applied Mechanics and Engineering 312:130–166.

[20] Borja RI (2000). A finite element model for strain localization analysis of strongly discontinuous fields based on standard Galerkin approxima-

tion. Computer Methods in Applied Mechanics and Engineering 190(11–12):1529–1549.

[21] Borja RI, Regueiro RA (2001). Strain localization in frictional materials exhibiting displacement jumps. Computer Methods in Applied Mechanics and Engineering 190(20–21):2555–2580.

[22] Borja RI, Aydin A (2004). Computational modeling of deformation bands in granular media, I: Geological and mathematical framework. Computer Methods in Applied Mechanics and Engineering 193(27–29):2667–2698.

[23] Borja RI (2004). Computational modeling of deformation bands in granular media. II. Numerical simulations. Computer Methods in Applied Mechanics and Engineering 193(27-29):2699–2718.

[24] Borja RI (2008). Assumed enhanced strain and the extended finite element methods: A unification of concepts. Computer Methods in Applied Mechanics and Engineering 197(33–34):2789–2803.

[25] Borja RI (2013), Plasticity Modeling & Computation, Springer-Verlag, Berlin Heidelberg.

[26] Borja RI, Yin Q, Zhao Y (2020). Cam-Clay plasticity. Part IX: On the anisotropy, heterogeneity, and viscoplasticity of shale. Computer Methods in Applied Mechanics and Engineering 360:112695.

[27] Borja RI, Chen W, Odufisan AR (2023). A constitutive framework for rocks undergoing solid dissolution. Journal of the Mechanics and Physics of Solids 173:105198.

[28] Bourdin B, Francfort GA, Marigo J-J (2000). Numerical experiments in revisited brittle fracture. Journal of the Mechanics and Physics of Solids 48(4):797–826.

[29] Braathen A, Petrie E, Nystuen T, Sundal A, Skurtveit E, Zuchuat V, Gutierrez M, Midtkandal I (2020). Interaction of deformation bands and fractures during progressive strain in monocline-San Rafael Swell, Central Utah, USA. Journal of Structural Geology 141:104219.

[30] Bryant EC, Sun, W (2018). A mixed-mode phase field fracture model in anisotropic rocks with consistent kinematics. Computer Methods in Applied Mechanics and Engineering 342:561–584.

[31] Cavailhes T, Rotevatn A (2018). Deformation bands in volcaniclastic rocks–Insights from the Shihtiping tuffs, Coastal Range of Taiwan. Journal of Structural Geology 113:155–175.

[32] Chemenda AI (2009). The formation of tabular compaction-band arrays: theoretical and numerical analysis. Journal of the Mechanics and Physics of Solids 57(5):851–868.

[33] Chemenda AI, Wibberley C, Saillet E (2012). Evolution of compactive shear deformation bands: Numerical models and geological data. Tectonophysics 526:56–66.

[34] Cheng P, Zhu H, Zhang Y, Jiao Y, Fish J (2022). Coupled thermo-hydro-mechanical-phase field modeling for fire-induced spalling in concrete. Computer Methods in Applied Mechanics and Engineering 389:114327.

[35] Choo J, Sun W (2018). Cracking and damage from crystallization in pores: Coupled chemo-hydro-mechanics and phase-field modeling. Computer Methods in Applied Mechanics and Engineering 335:347–379.

[36] Choo J, Sun W (2018). Coupled phase-field and plasticity modeling of geological materials: From brittle fracture to ductile flow. Computer Methods in Applied Mechanics and Engineering 330:1–32.

[37] Chu D, Li X, Liu Z, Cheng J, Wang T, Li Z, Zhuang Z (2019). A unified phase field damage model for modeling the brittle-ductile dynamic failure mode transition in metals. Engineering Fracture Mechanics 212:197–209.

[38] Cil MB, Hurley RC, Graham-Brady L (2020). Constitutive model for brittle granular materials considering competition between breakage and dilation. Journal of Engineering Mechanics 146(1): 04019110.

[39] Cilona A, Faulkner DR, Tondi E, Agosta F, Mancini L, Rustichelli A, Baud P, Vinciguerra S (2014). The effects of rock heterogeneity on compaction localization in porous carbonates. Journal of Structural Geology 67:75–93.

[40] Collins IF, Houlsby GT (1997). Application of thermomechanical principles to the modelling of geotechnical materials. Proceedings of the Royal Society of London. Series A: Mathematical, Physical and Engineering Sciences 453(1964): 1975-2001.

[41] Collins IF (2003). A systematic procedure for constructing critical state models in three dimensions. International Journal of Solids and Structures 40(17):4379–4397.

[42] Collins-Craft NA, Stefanou I, Sulem J, Einav I (2020). A Cosserat breakage mechanics model for brittle granular media. Journal of the Mechanics and Physics of Solids 141:103975.

[43] Das A, Nguyen GD, Einav I (2013). The propagation of compaction bands in porous rocks based on breakage mechanics. Journal of Geophysical Research: Solid Earth 118(5):2049–2066.

[44] Das A, Tengattini A, Nguyen GD, Viggiani G, Hall SA, Einav I (2014). A thermomechanical constitutive model for cemented granular materials with quantifiable internal variables. Part II–validation and localization analysis. Journal of the Mechanics and Physics of Solids 70:382–405.

[45] del Castillo EM, Fávero Neto AH, Borja RI (2021). Fault propagation and surface rupture in geologic materials with a meshfree continuum method. Acta Geotechnica 16:2463–2486.

[46] del Castillo EM, Fávero Neto AH, Borja RI (2021). A continuum meshfree method for sandbox-style numerical modeling of accretionary and doubly vergent wedges. Journal of Structural Geology 153:104466.

[47] Diehl P, Lipton R, Wick T, Tyagi M (2022). A comparative review of peridynamics and phase-field models for engineering fracture mechanics. Computational Mechanics, https://doi.org/10.1007/s00466-022-02147-0.

[48] Duan K, Kwok CY, Ma X (2017). DEM simulations of sandstone under true triaxial compressive tests. Acta Geotechnica 12(3):495–510.

[49] Eichhubl P, Hooker JN, Laubach SE (2010). Pure and shear-enhanced compaction bands in Aztec Sandstone. Journal of Structural Geology 32(12):1873–1886.

[50] Fei F, Choo J (2020). A phase-field model of frictional shear fracture in geologic materials. Computer Methods in Applied Mechanics and Engineering 369:113265.

[51] Fei F, Choo J (2021). Double-phase-field formulation for mixed-mode fracture in rocks. Computer Methods in Applied Mechanics and Engineering 376:113655.

[52] Feng D-C, Wu J-Y (2018). Phase-field regularized cohesive zone model (CZM) and size effect of concrete. Engineering Fracture Mechanics 197:66–79.

[53] Fortin J, Stanchits S, Dresen G, Guéguen Y (2006). Acoustic emission and velocities associated with the formation of compaction bands in sandstone. Journal of Geophysical Research: Solid Earth 111(B10).

[54] Fossen H, Schultz RA, Torabi A (2011). Conditions and implications for compaction band formation in the Navajo Sandstone, Utah. Journal of Structural Geology 33(10):1477–1490.

[55] Fossen H, Soliva R, Ballas G, Trzaskos B, Cavalcante C, Schultz RA (2018). A review of deformation bands in reservoir sandstones: geometries, mechanisms and distribution. Geological Society, London, Special Publications 459(1):99–33.

[56] Francfort GA, Marigo J-J (1998). Revisiting brittle fracture as an energy minimization problem. Journal of the Mechanics and Physics of Solids 46(8):1319–1342.

[57] Grady DE (1994). Dissipation in adiabatic shear bands. Mechanics of Materials 17(2-3):289–293.

[58] Hill R (1989). Analysis of deformation bands in the Aztec Sandstone, Valley of Fire State Park, Nevada, MS thesis, Univ. of Nevada, Las Vegas

[59] Holcomb D, Rudnicki JW, Issen KA, Sternlof K (2007). Compaction localization in the Earth and the laboratory: state of the research and research directions. Acta Geotechnica 2(1):1–15.

[60] Hu Z, Zhang H, Zheng Y, Ye H (2022). Phase-field implicit material point method with the convected particle domain interpolation for brittle–ductile failure transition in geomaterials involving finite deformation. Computer Methods in Applied Mechanics and Engineering 390:114420.

[61] Huang L, Baud P, Cordonnier B, Renard F, Liu L, Wong T-f (2019). Synchrotron X-ray imaging in 4D: multiscale failure and compaction localization in triaxially compressed porous limestone. Earth and Planetary Science Letters 528:115831.

[62] Ip SCY, Choo J, Borja RI (2021). Impacts of saturation-dependent anisotropy on the shrinkage behavior of clay rocks. Acta Geotechnica 16(11):3381–3400.

[63] Ip SCY, Borja RI (2022). Evolution of anisotropy with saturation and its implications for the elastoplastic responses of clay rocks. Interna-

tional Journal for Numerical and Analytical Methods in Geomechanics 46(1):23–46.

[64] Ip SCY, Borja RI (2022). A phase-field approach for compaction band formation due to grain crushing. International Journal for Numerical and Analytical Methods in Geomechanics 46(16):2965–2987.

[65] Ip SCY, Borja RI (2023). Multiscale interactions of elastic anisotropy in unsaturated clayey rocks using a homogenization model. Acta Geotechnica. https://doi.org/10.1007/s11440-022-01784-2.

[66] Issen KA, Rudnicki JW (2000). Conditions for compaction bands in porous rock. Journal of Geophysical Research: Solid Earth 105(B9):21529–21536.

[67] Jacquey AB, Regenauer-Lieb K (2021). Thermomechanics for geological, civil engineering and geodynamic applications: Rate-dependent critical state line models. Rock Mechanics and Rock Engineering 54(10):5355–5373.

[68] Jacquey, A. B., Regenauer-Lieb, K., & Cacace, M. (2021). Thermomechanics for geological, civil engineering and geodynamic applications: numerical implementation and application to the Bentheim sandstone. Rock Mechanics and Rock Engineering, 54(10), 5337-5354.

[69] Leuthold J, Gerolymatou E, Vergara MR, Triantafyllidis T (2021). Effect of compaction banding on the hydraulic properties of porous rock: part I—experimental investigation. Rock Mechanics and Rock Engineering 54(6):2671–2683.

[70] Liu C, Pollard DD, Deng S, Aydin A (2015). Mechanism of formation of wiggly compaction bands in porous sandstone: 1. Observations and conceptual model. Journal of Geophysical Research: Solid Earth 120(12): 8138–8152.

[71] Liu F, Borja RI (2008). A contact algorithm for frictional crack propagation with the extended finite element method. International Journal for Numerical Methods in Engineering 76(10):1489–1512.

[72] Liu F, Borja RI (2010). Stabilized low-order finite elements for frictional contact with the extended finite element method. Computer Methods in Applied Mechanics and Engineering 199(37–40):2456–2471.

[73] Liu S, Wang Y, Peng C, Wu W (2022). A thermodynamically consistent phase field model for mixed-mode fracture in rock-like materials. Computer Methods in Applied Mechanics and Engineering 392:114642.

[74] Liu Y, Borja RI (2022). Time scales in the primary and secondary compression of soils. International Journal for Numerical and Analytical Methods in Geomechanics 46(8):1383–1408.

[75] Louis L, Wong T-f, Baud P, Tembe S (2006). Imaging strain localization by X-ray computed tomography: discrete compaction bands in Diemelstadt sandstone. Journal of Structural Geology 28(5):762–775.

[76] Lubliner J (1972). On the thermodynamic foundations of non-linear solid mechanics. International Journal of Non-Linear Mechanics, 7(3): 237–254.

[77] Marinelli F, Buscarnera G (2019). Anisotropic breakage mechanics: From stored energy to yielding in transversely isotropic granular rocks. Journal of the Mechanics and Physics of Solids 129:1–18.

[78] Marketos G, Bolton MD (2009). Compaction bands simulated in discrete element models. Journal of Structural Geology 31(5):479–490.

[79] McAuliffe C, Waisman H (2016). A coupled phase field shear band model for ductile–brittle transition in notched plate impacts. Computer Methods in Applied Mechanics and Engineering 305:173–195.

[80] Miehe C, Hofacker M, Welschinger F (2010). A phase field model for rate-independent crack propagation: Robust algorithmic implementation based on operator splits. Computer Methods in Applied Mechanics and Engineering 199(45-48):2765–2778.

[81] Miehe C, Welschinger F, Hofacker M (2010). Thermodynamically consistent phase-field models of fracture: Variational principles and multi-field FE implementations. International Journal for Numerical Methods in Engineering 83(10):1273–1311.

[82] Miehe C, Hofacker M, Schänzel L-M, Aldakheel F (2015). Phase field modeling of fracture in multi-physics problems. Part II. Coupled brittle-to-ductile failure criteria and crack propagation in thermo-elastic–plastic solids. Computer Methods in Applied Mechanics and Engineering 294:486–522.

[83] Miehe C, Aldakheel F, Raina A (2016). Phase field modeling of ductile fracture at finite strains: A variational gradient-extended plasticity-damage theory. International Journal of Plasticity 84:1–32.

[84] Mollema PN, Antonellini MA (1996). Compaction bands: a structural analog for anti-mode I cracks in aeolian sandstone. Tectonophysics 267(1-4):209–228.

[85] Nguyen T K, Desrues J, Vo TT, Combe G (2022). FEMxEM multi-scale model for cemented granular materials: Inter- and intra-granular cracking induced strain localisation. International Journal for Numerical and Analytical Methods in Geomechanics 46(5):1001--1025.

[86] Olsson WA, Holcomb DJ (2000). Compaction localization in porous rock. Geophysical Research Letters 27(21):3537–3540.

[87] Olsson WA, Holcomb DJ, Rudnicki JW (2002). Compaction localization in porous sandstone: Implications for reservoir mechanics. Oil & Gas Science and Technology 57(5):591–599.

[88] Prassa C, Alevizos S, Veveakis M, Dafalias YF (2022). The influence of anisotropy on compaction bands: The case of coaxiality between stress and fabric anisotropy tensors. International Journal for Numerical and Analytical Methods in Geomechanics, 46(1):68--88.

[89] Rao S, Budzik MK, Dias MA (2022). On microscopic analysis of fracture in unidirectional composite material using phase field modelling. Composites Science and Technology 220:109242.

[90] Rudnicki JW (2004). Shear and compaction band formation on an elliptic yield cap. Journal of Geophysical Research: Solid Earth 109(B3).

[91] Rudnicki JW, Sternlof (2005). Energy release model of compaction band propagation. Geophysical Research Letters 32(L16303) doi:10.1029/2005GL023602.

[92] Rutqvist J (2012). The geomechanics of CO2 storage in deep sedimentary formations. Geotechnical and Geological Engineering 30(3):525–551.

[93] Sanz-Serna JM, Spijker MN (1986). Regions of stability, equivalence theorems and the Courant-Friedrichs-Lewy condition. Numerische Mathematik 49(2): 319–329.

[94] Semnani SJ, White JA, Borja RI (2016). On the strength of transversely isotropic rocks. International Journal for Numerical and Analytical Methods in Geomechanics 40(18):2423–2449.

[95] Semnani SJ, Borja RI (2017). Quantifying the heterogeneity of shale through statistical combination of imaging across scales. Acta Geotechnica 12(6):1193–1205.

[96] Shahin G, Marinelli F, Buscarnera G (2019). Viscoplastic interpretation of localized compaction creep in porous rock. Journal of Geophysical Research: Solid Earth 124(10): 10180-10196.

[97] Shahin G, Buscarnera G. (2020). Simulation of emergent compaction banding fronts caused by frictional boundaries. Géotechnique Letters 10(3): 436-444.

[98] Shahin G, Papazoglou A, Marinelli F, Viggiani G, Buscarnera G (2022). Experimental study of compaction localization in carbonate rock and constitutive modeling of mechanical anisotropy. International Journal for Numerical and Analytical Methods in Geomechanics 46(13):2561--2581.

[99] Simo JC (1998). Numerical analysis and simulation of plasticity. Handbook of Numerical Analysis 6:183–499.

[100] Stefanou I, Sulem J (2014). Chemically induced compaction bands: Triggering conditions and band thickness. Journal of Geophysical Research: Solid Earth 119(2):880–899.

[101] Stefanov YP, Chertov MA, Aidagulov GR, Myasnikov AV (2011). Dynamics of inelastic deformation of porous rocks and formation of localized compaction zones studied by numerical modeling. Journal of the Mechanics and Physics of Solids 59(11):2323–2340.

[102] Sternlof KR, Rudnicki JW, Pollard DD (2005). Anticrack inclusion model for compaction bands in sandstone. Journal of Geophysical Research: Solid Earth 110(B11).

[103] Suh HS, Sun W (2022). Multi-phase-field microporomechanics model for simulating ice-lens growth in frozen soil. International Journal for Numerical and Analytical Methods in Geomechanics, 46(12):2307--2336.

[104] Sun W, Kuhn MR, Rudnicki JW (2013). A multiscale DEM-LBM analysis on permeability evolutions inside a dilatant shear band. Acta Geotechnica 8(5):465–480.

[105] Sun W, Fish J, Liu F, Lu Y (2022) A stabilized two-phase PD-FEM coupling approach for modeling partially saturated porous media. Acta Geotech. (2022). https://doi.org/10.1007/s11440-022-01619-0

[106] Sweidan AH, Niggemann K, Heider Y, Ziegler M, Markert B (2022). Experimental study and numerical modeling of the thermo-hydro-mechanical processes in soil freezing with different frost penetration directions. Acta Geotechnics 17:231–255.

[107] Tembe S, Vajdova V, Wong T-f, Zhu W (2006). Initiation and propagation of strain localization in circumferentially notched samples of two porous sandstones. Journal of Geophysical Research: Solid Earth 111(B2).

[108] Tembe S, Baud P, Wong T-Af (2008). Stress conditions for the propagation of discrete compaction bands in porous sandstone. Journal of Geophysical Research: Solid Earth 113(B9).

[109] Truesdell C, Noll W (2004). The Non-linear Field Theories of Mechanics. Springer, Berlin Heidelberg.

[110] Vajdova V, Wong T-f (2003). Incremental propagation of discrete compaction bands: Acoustic emission and microstructural observations on circumferentially notched samples of Bentheim. Geophysical Research Letters 30(14).

[111] Wang T, Ye X, Liu Z, Chu D, Zhuang Z (2019). Modeling the dynamic and quasi-static compression-shear failure of brittle materials by explicit phase field method. Computational Mechanics 64(6):1537–1556.

[112] Wu J-Y (2017). A unified phase-field theory for the mechanics of damage and quasi-brittle failure. Journal of the Mechanics and Physics of Solids 103:72–99.

[113] Wu H, Guo N, Zhao J (2018). Multiscale modeling and analysis of compaction bands in high-porosity sandstones. Acta Geotechnica 13(3):575–599.

[114] Wu J-Y, Nguyen VP, Nguyen CT, Sutula D, Sinaie S, Bordas SPA (2020). Phase-field modeling of fracture. Advances in Applied Mechanics 53:1–183.

[115] Wu JY, Chen WX, Zhou H (2022). A length scale insensitive phase-field model for fully coupled thermo-mechanical fracture in concrete at high temperatures. International Journal for Numerical and Analytical Methods in Geomechanics 46(14):2725–2753.

[116] Wu H, Papazoglou A, Viggiani G, Dano C, Zhao J (2020). Compaction bands in Tuffeau de Maastricht: insights from X-ray tomography and multiscale modeling. Acta Geotechnica 15(1):39–55.

[117] Xu Z, He X, Han Y, Huang F (2020). A different viewpoint on mechanism of fracture to shear-banding failure mode transition. Journal of the Mechanics and Physics of Solids 145:104165.

[118] Xu Y, Ming P, Chen J (2020). A phase field framework for dynamic adiabatic shear banding. Journal of the Mechanics and Physics of Solids 135:103810.

[119] Xu Y, Zhou S, Xia C, Hu Y (2022). A new phase field model for mixed-mode brittle fractures in rocks modified from triple shear energy criterion. Acta Geotechnica (2022). https://doi.org/10.1007/s11440-022-01589-3

[120] Yang J, Tchelepi HA, Kovscek AR (2021). Phase-field modeling of rate-dependent fluid-driven fracture initiation and propagation. International Journal for Numerical and Analytical Methods in Geomechanics, 45(8):1029–1048.

[121] You T, Waisman H, Zhu Q-Z (2021). Brittle-ductile failure transition in geomaterials modeled by a modified phase-field method with a varying damage-driving energy coefficient. International Journal of Plasticity 136;102836.

[122] Zeng Q, Wang T, Zhu S, Chen H, Fang D (2022). A rate-dependent phase-field model for dynamic shear band formation in strength-like and toughness-like modes. Journal of the Mechanics and Physics of Solids 164:104914.

[123] Zhang P, Feng Y, Bui TQ, Hu X, Yao W (2020). Modelling distinct failure mechanisms in composite materials by a combined phase field method. Composite Structures 232:111551.

[124] Zhang H, Pei X-Y, Peng H, Wu J-Y (2021). Phase-field modeling of spontaneous shear bands in collapsing thick-walled cylinders. Engineering Fracture Mechanics 249:107706.

[125] Zhang Q, Borja RI (2021). Poroelastic coefficients for anisotropic single and double porosity media. Acta Geotechnica 16, 3013–3025.

[126] Zhao Y, Borja RI (2020). A continuum framework for coupled solid deformation-fluid flow through anisotropic elastoplastic porous media. Computer Methods Applied Mechanics and Engineering 369:113225.

[127] Zhao Y, Semnani SJ, Yin Q, Borja RI (2018). On the strength of transversely isotropic rocks. International Journal for Numerical and Analytical Methods in Geomechanics 42(16):1917–1934.

[128] Zhao Y, Borja RI (2022). A double-yield-surface plasticity theory for transversely isotropic rocks. Acta Geotechnica 17;5201–5221.

[129] Zhou S, Zhuang X (2020). Phase field modeling of hydraulic fracture propagation in transversely isotropic poroelastic media. Acta Geotechnica 15(9):2599–2618.

[130] Ziegler H (2012). An introduction to Thermomechanics, Elsevier.